Journal of Colloid and Interface Science 678 (2025) 210–226

Contents lists available at ScienceDirect

Journal of Colloid And Interface Science

journal homepage: www.elsevier.com/locate/jcis

Regular Article

Ultrafast microwave synthesis of MoSSe@ graphene composites via dual anion design for long-cyclable Li-S batteries

Zhen Wei [a], Shatila Sarwar [b], Xinyu Zhang [b,*], Ruigang Wang [c,*]

[a] Department of Metallurgical and Materials Engineering, The University of Alabama, Tuscaloosa, AL 35487, United States
[b] Department of Chemical Engineering, Auburn University, Auburn, AL 36849, United States
[c] Department of Chemical Engineering and Materials Science, Michigan State University, East Lansing, MI 48824, United States

GRAPHICAL ABSTRACT

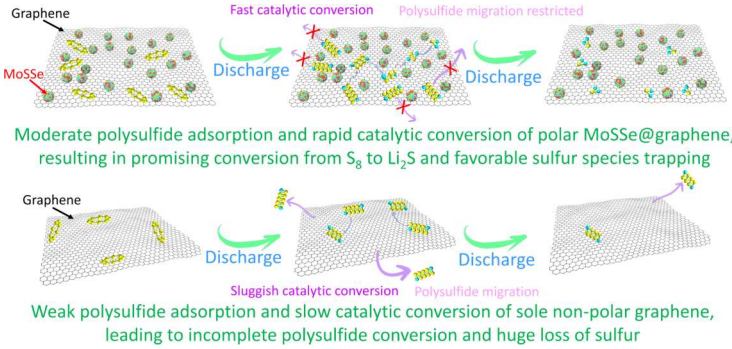

ARTICLE INFO

Keywords:
Li-S batteries
Transition-metal dichalcogenides
Nanohybrid engineering
Sulfiphilicity-lithiophilicity
Ultrafast microwave synthesis

ABSTRACT

Lithium-sulfur batteries (LSBs) have been increasingly recognized as a promising candidate for the next-generation energy-storage systems. This is primarily because LSBs demonstrate an unparalleled theoretical capacity and energy density far exceeding conventional lithium-ion batteries. However, the sluggish redox kinetics and formidable dissolution of polysulfides lead to poor sulfur utilization, serious polarization issues, and cyclic instability. Herein, sulfiphilic few-layer MoSSe nanoflake decorated on graphene (MoSSe@graphene), a two-dimensional and catalytically active hetero-structure composite, was prepared through a facile microwave method, which was used as a conceptually new sulfur host and served as an interfacial kinetic accelerator for LSBs. Specifically, this sulfiphilic MoSSe nanoflake not only strongly interacts with soluble polysulfides but also dynamically promotes polysulfide redox reactions. In addition, the 2D graphene nanosheets can provide an extra physical barrier to mitigate the diffusion of lithium polysulfides and enable much more uniform sulfur distribution, thus dramatically inhibiting polysulfides shuttling meanwhile accelerating sulfur conversion reactions. As a result, the cells with MoSSe@graphene nanohybrid achieved a superior rate performance (1091 mAh/g at 1C) and an ultralow decaying rate of 0.040 % per cycle after 1000 cycles at 1C.

* Corresponding authors.
E-mail addresses: xzz0004@auburn.edu (X. Zhang), rwang@msu.edu (R. Wang).

https://doi.org/10.1016/j.jcis.2024.09.048
Received 21 June 2024; Received in revised form 3 September 2024; Accepted 4 September 2024
Available online 8 September 2024

1. Introduction

Energy storage has become a fundamental need and an important issue concerning our daily life [1,2]. The continuous consumption of fossil fuels has led to "carbon accumulation" in the natural cycles. The tremendous amount of CO_2 generated from anthropogenic activities is considered as the primary contributor of greenhouse gases, resulting in significant environmental changes. To mitigate CO_2 emission, there is an increasing demand for electrochemical energy storage systems with the benefits of near-zero carbon emission, including batteries [3], solar cells [4], and supercapacitors (SCs) [5,6]. With the rapid growth of electric vehicles market, currently, Li-ion batteries are reaching their energy density limit and can hardly meet the increasing demands for high-performance energy storage, which has triggered growing fundamental research and development of novel rechargeable batteries. Among the next-generation rechargeable batteries, Li-S battery has caught ever-increasing attention from researchers owing to its impressive high theoretical capacity of 1675 mAh g^{-1} and energy density of 2600 Wh kg^{-1} (much higher than 200-400 Wh kg^{-1} of Li-ion batteries). These attributes, coupled with the environmental friendliness, abundant resources, and relatively low cost of sulfur, underscore the potential of Li-S batteries as a promising candidate for the next-generation power sources. However, the parasitic "shuttle effect" caused by the migration of soluble polysulfides leads to 1) low S utilization, 2) poor Coulombic efficiency, and 3) rapid capacity degradation, which is considered as the most formidable technical challenge for the commercialization of Li-S batteries. Numerous technical strategies have been attempted to address the polysulfide shuttling issue. For instance, various highly conductive carbonaceous materials, including mesoporous carbon [7], graphene [8], carbon nanotubes [9], and polyaniline [10], etc. were used as sulfur host materials for improving the intrinsic insulating characteristics of elemental sulfur and discharge products (i.e., lithium sulfide), meanwhile physically adsorbing ("trap") polysulfides due to their high surface area of such carbonaceous host materials [11].

Although carbonaceous materials typically demonstrate significant capacity improvement over the first few cycles, they still suffer from fast capacity fading upon elongated cycling owing to the incapability of constructing the strong chemical interaction between polysulfides and carbon [12]. Therefore, chemical adsorption must be considered for immobilizing the soluble polysulfides by forming stronger chemical bonds. Numerous polar materials such as TiO_2 [13], SnO_2 [14], MnO_2 [15], and V_2O_5 [16] with various innovatively designed structures have been investigated to impede polysulfide diffusion during cycling. Even though these strategies (via physical or chemical adsorption) can improve the electrochemical performances of Li-S batteries to some extent, Li-S batteries still suffer from the sluggish conversion kinetics between soluble polysulfides and insoluble solid phases (i.e., sulfur and Li_2S), degrading the rate performance and limiting the efficient utilization of active materials.

Recently, transition-metal dichalcogenides (TMDCs), a class of compounds that possess good chemical stability and unique microstructures, have garnered significant attention in the scientific community used as electrocatalysts in sulfur cathode of Li-S batteries to further mitigate the polysulfides shuttling. It is noted that the basal plane of semiconducting TMDCs exhibits only ordinary lithiophilicity and sulfiphilicity, resulting in an unsatisfactory catalytic activity and lithium deposition.

To address these issues and further enhance the performance of TMDCs, dual-anion MoSSe were designed and fabricated in this work. This was achieved through a partial substitution of S atoms with Se atoms, a process aimed at generating a plethora of anion vacancies. The introduction of these anion vacancies has dual effects: it imparts the lithiophilicity and sulfiphilicity of TMDCs and the presence of anion vacancies also leads to a reduction in the band gap, significantly enhancing the electronic conductivity and facilitating the ion diffusion kinetics.

The effective combination of metal chalcogenides with highly conductive supports, such as graphene, reduced graphene oxide (rGO), carbon nanotubes (CNT), and others, is paramount in preventing the formidable aggregation of transition metal chalcogenide (TMC) layers. Therefore, a few Janus-type MoSSe compounds have been hybridized with highly conductive supports [17]. Additionally, hydrothermal [18], solvothermal [19], and chemical vapor deposition (CVD) [20] are commonly used to fabricate such TMC nanohybrids. Nevertheless, these approaches above require complex synthetic procedures and a large amount of energy consumption. Therefore, it is necessary to develop a facile strategy to fabricate the TMC-based composites with favorable electrocatalytic activity.

In this study, we prepared molybdenum sulfoselenide compounds with highly conductive graphene as support (MoSSe@graphene) via an ultrafast (60 s) microwave-assisted heating method and further used MoSSe@graphene composites as electrocatalysts to accelerate the conversion between soluble polysulfides to insoluble Li_2S/Li_2S_2. The preparation procedures are briefly illustrated in Fig. 1**a**. In contrast to other traditional methods, microwave-assisted heating has several promising merits such as faster volumetric heating, accelerated reaction rate, improved purity, enhanced selectivity, reduced reaction time, and increased product yields. **Table S1** compares some advantages and disadvantages between the microwave-assisted and conventional heating methods.

2. Experimental section

2.1. Materials and reagents

Ammonium tetrathiomolybdate, specifically with a chemical formula $(NH_4)_2MoS_4$ (purity: 99.95 %), was purchased from BeanTown Chemical, Inc. Carbon disulfide (CS_2, with a purity of 99.9 %), was sourced from Alfa Aesar. Selenium powder, with a particle size of approximately 325 mesh, and polyvinylidene fluoride (PVDF) were also obtained from Alfa Aesar. Graphene powder was supplied by Magnolia Ridge Inc. Furthermore, carbon cloth, measuring 20 cm × 20 cm, with a thickness of 0.381 mm and a density of 1.75 g/cm^3, was purchased from Fuel Cell Earth LLC. This carbon cloth serves as a current collector. All the chemicals purchased were utilized precisely as they were received, without any additional processing or purification steps.

2.2. The synthesis of MoSSe@graphene

MoSSe@graphene compound was meticulously prepared via a ultrafast microwave method, as shown in Fig. 1**a**, through the chemical reaction of ammonium tetrathiomolybdate (ATTM), CS_2 solvent, and selenium (Se) powder on a graphene substrate. To achieve a well-balanced mixture, equal amounts (15 mg each) of ATTM, graphene, and selenium (Se) powder were combined in a glass vial. The mixture powder was thoroughly homogenized using a Vortex mixer, which was set at a consistent speed of 2000 rpm. Shortly after that, CS_2 solvent (200 μL) was introduced to the mixture and thoroughly blended once again at 2000 rpm. After the blending, the solvent was air-dried for 10 min. Subsequently, the homogenous dry blend of ATTM-graphene-CS_2-Selenium was exposed to microwave radiation within a conventional microwave oven, operating at a frequency of 2.45 GHz and delivering a power output of 1250 W, for a total duration of 60 s. The inclusion of graphene within this mixture plays a dual role: first, it serves as an ideal platform, or substrate, for efficient absorption of microwave energy; second, it facilitates the transformation of the microwave energy into a localized heat source. Specifically, the intense heat accelerated the reduction of ATTM to form MoO_2, which was then further reduced to the target product, MoSSe, dispersed evenly across the graphene substrate.

Additionally, due to the localized hot spots, this process stimulated the release of any excess or residual constituents in the form of gaseous byproducts. It's worth emphasizing that incorporating graphene within

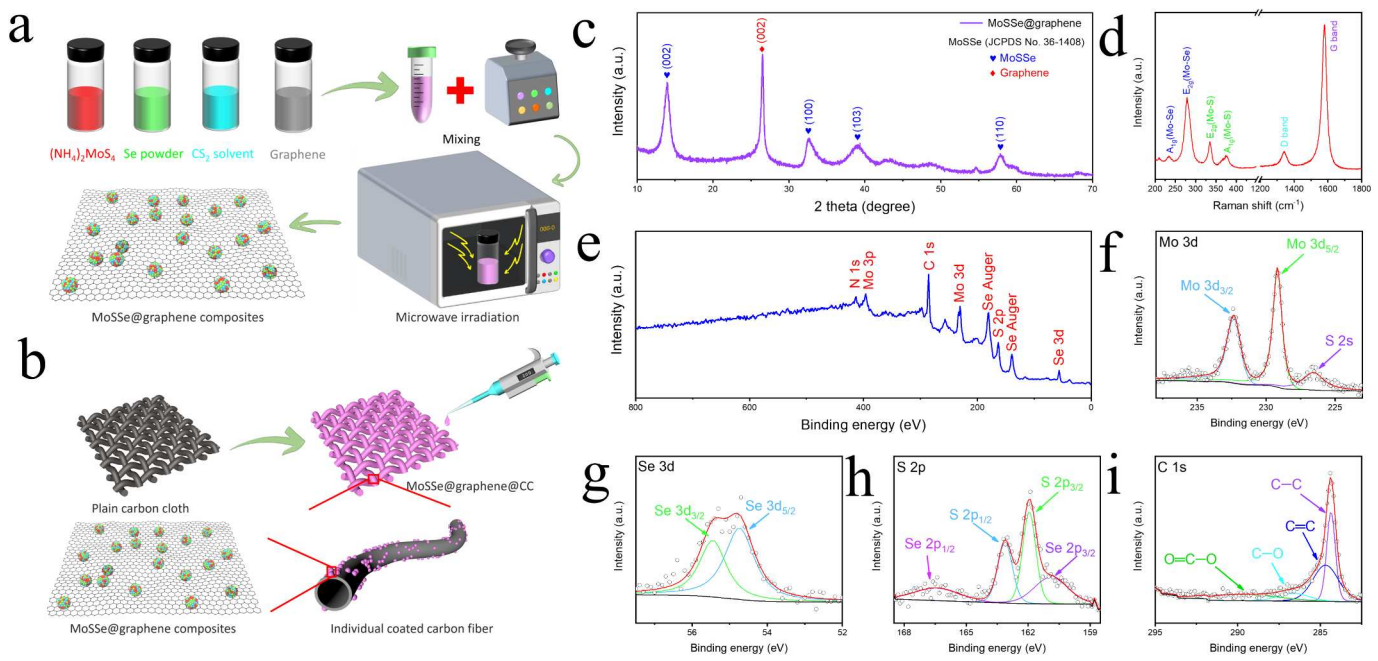

Fig. 1. Schematic illustration of the preparation procedure of (a) MoSSe@graphene composite by fast microwave irradiation and (b) MoSSe@graphene@CC electrodes by a simple slurry drop casting; (c) XRD, (d) Raman spectroscopy, and (e) XPS survey spectra of the MoSSe@graphene composite sample; (f) high-resolution XPS spectra of Mo 3d, (g) Se 3d, (h) S 2p, and (i) C 1s from (e).

the mixture was paramount in ensuring that the desired synthetic reactions occurred smoothly and efficiently. Its unique characteristics, including high thermal conductivity and superior ability to serve as a microwave susceptor, enabled the generation of localized heat, thereby driving the conversion of diverse precursor materials into the final product, MoSSe, in a timely and effective manner. Moreover, graphene also functions as a high surface area and outstanding conductive support for MoSSe nanosheets and hinders the aggregation of MoSSe nanosheets. All of these result in a significantly increased electrical conductivity and enlarged surface area of the as-synthesized MoSSe@graphene powders.

2.3. Physicochemical characterization

To probe into the crystal structure of the MoSSe@graphene composites, X-ray diffraction (XRD) patterns were collected on a Philips X'pert MPD diffractometer, equipped with Cu Kα radiation (wavelength $\lambda = 1.54056$ Å) operated at a high voltage of 45 kV and a current of 40 mA. Additionally, a Horiba Labram HR 800 Raman Spectrometer, equipped with a 532 nm laser module, was utilized to gather Raman spectra of the MoSSe@graphene composites. The Raman scattering was captured within the range of 200 to 1800 cm^{-1}. For each spectrum, an exposure time of 10 s and 10 cycles of accumulation were employed. A silicon single crystal wafer, presenting a distinct reference peak at 520.7 cm^{-1}, was utilized to calibrate the Raman spectrometer. The morphology and chemical compositions of the powders and cell components were comprehensively characterized using a scanning electron microscope (SEM, FE-Apreo) operated at an acceleration voltage of 20 kV and coupled with an energy dispersive X-ray spectrometer (EDS, EDAX Instruments).

Furthermore, an FEI Tecnai F20 transmission electron microscope (TEM) was employed for a more detailed structural and chemical analysis. This instrument was operated at an acceleration voltage of 200 kV and equipped with an EDAX EDS detector and a GIF (Gatan Image Filter) for spectroscopy analysis. X-ray photoelectron spectroscopy (XPS) was carried out for analyzing the surface chemical composition on a Kratos Axis Ultra DLD spectrometer. This instrument utilizes a monochromatic Al Kα radiation, which has a photon energy of 1486.6 eV, under ultra-high vacuum (10^{-10} Torr).

2.4. Preparation of Li_2S_6 solution

1 M bistrifluoromethanesulfonylimide (LiTFSI) (Adipogen Corp Ms, ≥ 99 %) in 1, 2-dimethoxyethane (DME) (Alfa Aesar, 99 %) and 1, 3-dioxolane (DOL) (Alfa Aesar, 99 %) in a 1:1 volume ratio with the addition of 0.5 M $LiNO_3$ (Alfa Aesar, 99.999 %) was used as the electrolyte. The elemental sulfur (Alfa Aesar, ≥ 99.5 %) was directly reacted with stoichiometric Li_2S (Alfa Aesar, ≥ 99.9 %) (the S/Li_2S molar ratio was 5:1) in the prepared electrolyte at 60 °C for 48 h. As a result of this reaction, a catholyte solution containing 1 M Li_2S_6 was formed, in which the concentration of Li_2S_6 was calculated based on sulfur. The final Li_2S_6 solution exhibited a brownish-red color and showed no obvious sedimentation.

2.5. Preparation of MoSSe@graphene@CC electrode and graphene@CC electrode

To evaluate the electrochemical performances of the Li-S cells, the cathodes were fabricated using carbon cloth (CC) as the current collector. Before coating with the MoSSe@graphene and graphene, CC were immersed in a 6 M HNO_3 solution for 8 h, followed by a thorough rinsing with deionized (DI) water and a subsequent drying process in a vacuum oven maintained at 60 °C for 60 min. This pretreatment aimed to ensure the removal of any surface residual impurities. In this research, CC was chosen as both the current collector and the substrate. This selection was primarily influenced by its remarkable electronic conductivity and mechanical strength. Commercially available CC was punched into circular discs with a diameter of 12 mm. The MoSSe@graphene@CC electrodes and graphene@CC electrodes were prepared through a straightforward surface coating method, as depicted in Fig. 1**b**. Employing a mixture with a specific mass ratio of 70 % MoSSe@graphene composite or pure graphene powder, 20 % Super P carbon black, and 10 % PVDF, all components were blended in *N*-methylpyrrolidone (NMP) which served as a solvent. Then the as-prepared MoSSe@graphene or graphene slurry were cast on the pretreated CC. The CC was again subjected to vacuum drying at a controlled temperature of 60 °C for 12 h. The areal mass loading of the as-synthesized MoSSe@graphene and the graphene powder was found to be

approximately 0.5 mg cm^{-2}.

2.6. Cell assembly and electrochemical measurements

To assemble CR2032 Li-S coin cells, the MoSSe@graphene and the graphene loaded cathodes were impregnated with a calculated volume of the 1 M Li_2S_6-containing catholyte. They were further paired with a high-purity Li metal anode and a Celgard separator and added with the electrolyte (1 M LiTFSI and 0.5 M $LiNO_3$ in 1:1 vol ratio of DOL to DME). The sulfur loading was determined by adjusting the quantity of the Li_2S_6 catholyte added to the cathode. For electrochemical cycling with a low sulfur loading, 6 μL Li_2S_6-containing catholyte was dropped onto the MoSSe@graphene@CC or graphene@CC cathodes (diameter: 12 mm and area: 1.13 cm^2) with 15 μL mg^{-1} (E/S: electrolyte/sulfur) of electrolyte in which 6 μL Li_2S_6 for 1 mg cm^{-2} of equivalent sulfur normalized to the cathode area. To achieve a high sulfur loading of 6 mg cm^{-2} under low electrolyte conditions, 36 μL of 1 M Li_2S_6-containing catholyte corresponding to 6 mg cm^{-2} of equivalent sulfur were dropped on the electrode. An appropriate amount of the electrolyte was dropped on the electrode where the E/S ratio was controlled at 8 μL mg^{-1}. It was further paired with a separator and Li metal anode. All the Li-S batteries were assembled in an Ar filled glove box ($O_2 < 0.1$ ppm, $H_2O<0.1$ ppm). All the as-assembled Li-S batteries were subjected to activation processes before various electrochemical measurements. Galvanostatic charge and discharge experiments were carried out by a NEWARE battery tester at various currents in the voltage range of 1.7–2.8 V (vs Li^+/Li). Cyclic voltammetry (CV) measurements and chronoamperometric curves were implemented on a Gamry Potentiostat/Galvanostat workstation (Gamry Interface 1000E) at various scan rates between 1.7 and 2.8 V. Electrochemical impedance spectroscopy (EIS) experiments were carried out and results were collected on the same Gamry Interface 1000E.

2.7. Measurements for the Li_2S nucleation

Li_2S_8 cells were assembled with a cathode (the MoSSe@graphene@CC or the graphene@CC electrode), a Li metal anode, and a Celgard 2400 separator. A 0.5 M Li_2S_8 solution was prepared by mixing sublimed S powder and Li_2S, maintaining a precise molar ratio of 7:1, and then dissolving this mixture in a DME and DOL solution, with a volume ratio of 1:1, which contained an additional 1.0 M LiTFSI. The solution was stirred vigorously to ensure complete dissolution and uniformity. In the experimental setup, 25 μL of the Li_2S_8 catholyte was carefully dropped onto the cathode, and an equivalent volume of 25 μL of conventional LiTFSI electrolyte was added to the anode side. The cells were then discharged galvanostatically to 2.06 V at a current of 0.112 mA and kept potentiostatically at 2.05 V, a potential that was specifically chosen to promote the nucleation of Li_2S. This step was maintained until the current decreased to an extremely low value of below 10^{-5} A. The nucleation rate of Li_2S on the different reactive electrode surfaces was calculated based on Faraday's law. As the control subject, the graphene@CC electrode was a substitute for the MoSSe@graphene@CC electrode with the other same experimental conditions and procedures.

2.8. Dissolution measurement of Li_2S

The investigation of Li_2S dissolution was conducted through assembling a series of new coin cells, which were subsequently subjected to a galvanostatic discharge at 0.10 mA until 1.7 V. This specific voltage was chosen to ensure the complete transformation of the sulfur species present within the cell into the solid state of Li_2S. Subsequently, the cells were subjected to a potentiostatic charging process, held at a consistent voltage of 2.35 V. This specific voltage was chosen to initiate the dissolution of the solid Li_2S into soluble polysulfides. This process was carried out until the charge current diminished to a negligible value of less than 10^{-5} A.

2.9. Symmetric cell assembly

The electrodes were prepared by thoroughly mixing host materials (MoSSe@graphene or pure graphene powder) with polyvinylidene fluoride (PVDF) in a weight ratio of 9:1. The mixture was then immersed in *N*-methyl-2-pyrrolidone (NMP) solvent to form a viscous slurry. Subsequently, the slurry was meticulously coated onto the free-standing carbon cloth discs, each having a uniform diameter of 12 mm. The slurry was then allowed to dry at a constant temperature of 60 °C for 12 h, ensuring that the solvent was completely evaporated. The mass loading of the active material was precisely controlled, ensuring that it was approximately 1.0 mg cm^{-2}. A 0.5 M solution of Li_2S_6 electrolyte was prepared by vigorously stirring sulfur and lithium sulfide in the electrolyte. The electrolyte used was a combination of 1 M bis(trifluoromethanesulfonyl)imide lithium salt (LiTFSI) and a mixture of diol (DOL) and dimethoxyethane (DME) in a volume ratio of 1:1. This stirring was carried out in an argon-filled glove box for a prolonged time. To assemble the 2032-type coin cell, two identical electrodes, prepared as previously described, were used, one serving as the cathode and the other as the anode. These electrodes were separated by a Celgard 2400 PP separator and held together by a 20 μL of the 0.5 M Li_2S_6 electrolyte. Cyclic voltammetry (CV) measurements of these symmetric cells were then conducted, employing a voltage range between −1.5 to 1.5 V and a scan rate of 0.5 mV/s.

2.10. Visualized polysulfide adsorption experiment

The visualized polysulfide adsorption experiment was implemented by utilizing a Li_2S_6 solution, which served as a representative example of polysulfides. A 1.5 mM Li_2S_6 solution was prepared by dispersing sulfur powder and lithium sulfide (Li_2S), maintaining a strict molar ratio of 1:5, into a mixed solvent of DME and DOL. The specific volume ratio of the solvents used was 1:1. Subsequently, the solution was vigorously stirred within an Argon-filled glovebox at ambient room temperature. This process was continued until a homogenous solution was achieved. The MoSSe@graphene composite and pure graphene powder, each weighing an identical 15 mg, were separately introduced into 2 mL of the 1.5 mM Li_2S_6 solution. Photos were captured at the beginning of the test and then again after a 2-hour interval of adsorption. At the culmination of this 2-hour adsorption period, the ultraviolet visible (UV–Vis) absorption spectra were collected.

2.11. Measurement of the galvanostatic intermittent titration (GITT)

The GITT experiment was executed to understand the kinetic effect. This experiment incorporated a precise current pulse protocol, which was set at 0.2C for 25 min, followed by a resting period of 15 min. The internal resistance of the battery can be quantitatively assessed by using the following relation equation:

$$\Delta R_{internal} = |\Delta V_{QOCV-CCV}| / I_{applied}$$

In this equation, $\Delta V_{QOCV\text{-}CCV}$ represents the voltage difference between two points: the quasi open-circuit voltage (QOCV) and the closed-circuit voltage (CCV). $I_{applied}$, on the other hand, denotes the current being applied to the battery cell during the experiment.

2.12. Shuttle current measurement

In a routine experiment, the cells without $LiNO_3$ additive were subjected to a galvanostatic charging and discharging process for three cycles. This was done at a low current density of 0.2C, to activate the cell. Subsequently, the cells were charged up to a voltage of 2.8 V and then allowed to discharge to a voltage of 2.38 V. This was done at a current density of 0.1C. Following this, the Li-S cells were shifted to a potentiostatic mode of operation, at which point the shuttle current

reached its peak value. It's worth noting that after approximately 104 s, the potentiostatic current stabilized. This can be accurately measured and recorded as the shuttle current for further analysis.

3. Results and discussion

3.1. Characterizations before cell cycling

The crystal structure of the MoSSe@graphene composite was analyzed by performing X-ray diffraction (XRD). Fig. 1**c** exhibits the XRD pattern of the prepared MoSSe@graphene composite powder. The distinct diffraction peaks, centered at 13.7°, 32.4°, 38.6°, and 57.5°, can be indexed to the (002), (100), (103), and (110) crystal planes of MoSSe (JCPDS 36–1408 [21]), correspondingly. The as-prepared MoSSe nanosheets demonstrate characteristic hexagonal 2H-molybdenum dichalcogenide features. The distinctive diffraction peak, at 26.5°, can be attributed to the (002) crystal plane of graphene [22].

The Raman spectrum of the MoSSe@graphene powder reveals the presence of in-plane E_{2g} and out-of-plane A_{1g} vibrations associated with the Mo-Se bonding at 281 and 233 cm^{-1}, respectively. Similar vibrations for the Mo–S bonding were observed at slightly higher frequencies of 335 and 374 cm^{-1} (Fig. 1**d**) [23]. The spectrum also showcases the presence of disordered (D band) and graphitic (G band) modes inherent to the graphene itself, manifesting at 1341 cm^{-1} and 1580 cm^{-1}, respectively [24].

The survey XPS spectrum, as illustrated in Fig. 1**e**, presents a comprehensive overview of the surface elemental constituents (carbon, molybdenum, sulfur, and selenium) of the MoSSe@graphene composite powder. The high-resolution XPS Mo 3d spectrum, depicted in Fig. 1**f**, unveils two prominent peaks at 229.2 and 232.4 eV. These peaks can be ascribed to the Mo $3d_{5/2}$ and Mo $3d_{3/2}$ spin–orbit doublets of Mo^{4+}, respectively [25]. Additionally, the peak at 226.5 eV can be assigned to the S 2 s orbital. The Se 3d spectrum of the MoSSe@graphene composite powder, as captured in Fig. 1**g**, showcases two noticeable peaks at 54.7 and 55.5 eV. These peaks are correlated to the Se $3d_{5/2}$ and Se $3d_{3/2}$ spin–orbit doublets, respectively, thereby confirming the presence of selenium in the MoSSe@graphene composite powder [26]. Moreover, the high-resolution S 2p spectrum of the MoSSe@graphene composite powder (Fig. 1**h**) demonstrates two observable peaks at 162.0 and 163.1 eV, which are associated with the S $2p_{3/2}$ and S $2p_{1/2}$ spin–orbit doublets, respectively. Additionally, the Se $2p_{3/2}$ and Se $2p_{1/2}$ peaks (Fig. 1**h**) of the MoSSe@graphene composite powder situated at 160.8 and 166.5 eV, respectively, further substantiate the existence of Se. The resolved C 1s spectrum of the MoSSe@graphene powder (Fig. 1**i**) shows the presence of four components: C—C (284.4 eV), C═C (284.7 eV), C—O (286.7 eV), and O═C–O (289.3 eV) [27].

Fig. 2**a** exhibits the SEM morphological structure of the MoSSe@-graphene composite powder. The MoSSe nanosheets are evenly distributed and embedded in the highly conductive graphene and there is no significant agglomeration. With the assistance of graphene, MoSSe preferentially adheres to the surface of conductive graphene rather than forming aggregates. These two 2D materials, MoSSe nanosheets and graphene, are homogeneously integrated into a 3D composite structure with larger surface area, exhibiting favorably synergistic effects: strong polysulfides capture on adsorptive sites and facile charge transfer on conductive sites. Fig. 2**b** exhibits the EDS mapping overlay of the MoSSe@graphene composite and Fig. 2**c** displays the individual EDS elemental mapping. It can be observed that C is uniformly distributed while Mo, S, and Se are mainly concentrated on the nanosheet-like structure, confirming that the MoSSe nanosheets are successfully anchored on the surface of the graphene.

TEM images of the MoSSe@graphene composite are shown in Fig. 2**d-e**. Fig. 2**d-e** demonstrate that the prepared graphene has very thin and wrinkled 2D sheet-like morphology. As demonstrated in Fig. 2**d-e**, the MoSSe@graphene composite contains a combination of MoSSe nanosheets and graphene, while the MoSSe nanosheet is firmly anchored on the graphene sheet with no significant aggregation. Fig. 2**f** exhibits the high-resolution TEM image of the MoSSe@graphene composite, in which the lattice fringe observed is about 0.65 nm (Fig. 2**f**), corresponding to the (002) crystal planes of MoSSe [28].

3.2. Electrochemical measurements

Cyclic voltammetry (CV) test can provide valuable insights into the underlying working mechanism of electrochemical reactions inside the rechargeable Li-S battery. Fig. 3**a** demonstrates the cyclic voltammogram curves of the Li-S batteries with the MoSSe@graphene@CC electrode and graphene@CC electrode in the voltage range of 1.7–2.8 V at a

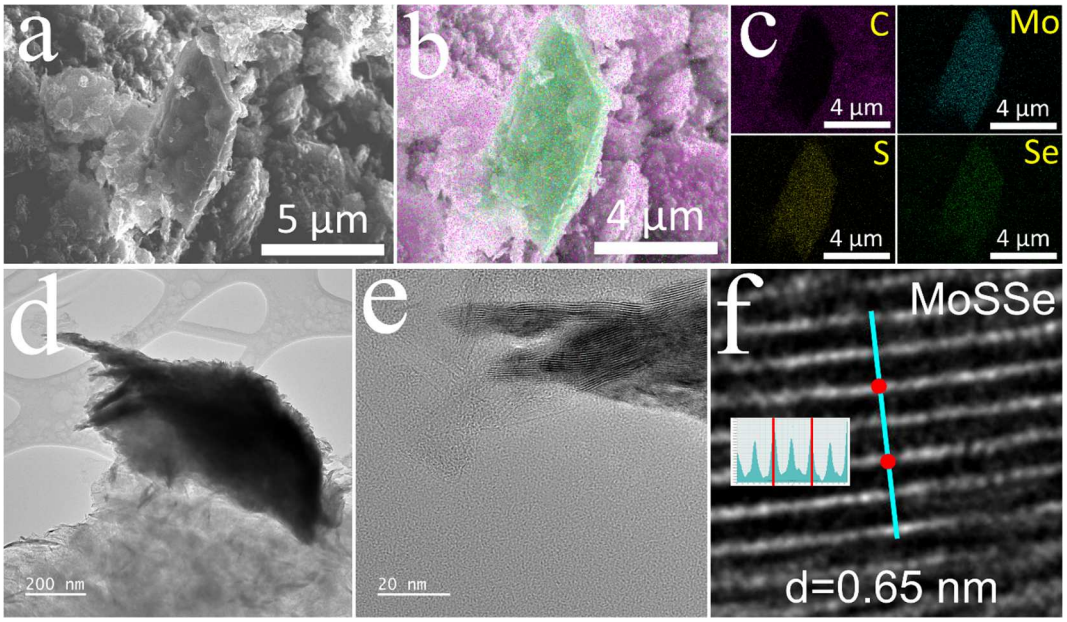

Fig. 2. (a) SEM image, (b) EDS mapping overlay, and (c) individual EDS elemental mapping of carbon (pink), molybdenum (blue), sulfur (yellow), and selenium (green) for the MoSSe@graphene sample; (d) TEM and (e) HRTEM images for the MoSSe@graphene sample; (f) The corresponding lattice spacing analysis. (For interpretation of the references to color in this figure legend, the reader is referred to the web version of this article.)

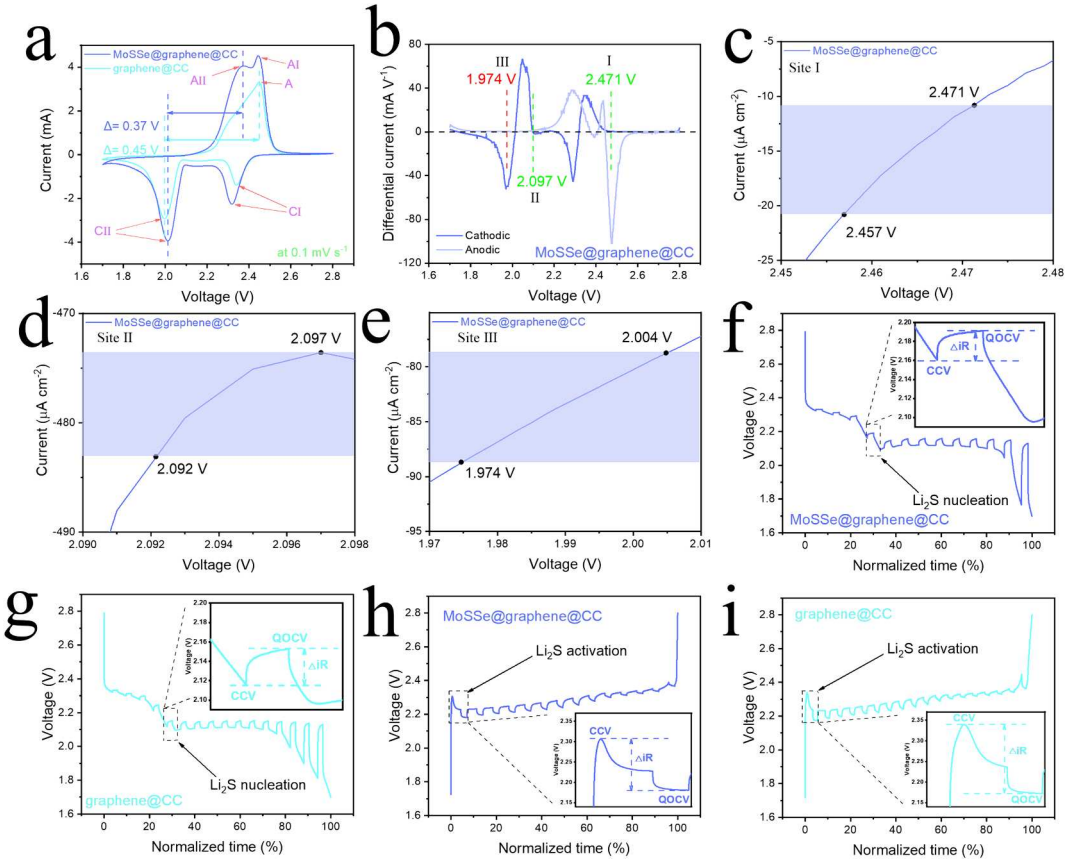

Fig. 3. (a) CV curves of the MoSSe@graphene@CC and the graphene@CC cells during the first scan at 0.1 mV s^{-1}; Differential CV curves of (b) MoSSe@graphene@CC cathode and corresponding onset potentials of the redox peaks I, II, and III are shown in (c-e). Galvanostatic intermittent titration (GITT) discharge profiles of (f) MoSSe@graphene@CC cathode and (g) graphene@CC cathode at 0.2C with respect to the normalized discharge − charge time. GITT charge profiles of (h) MoSSe@graphene@CC and (i) graphene@CC cathodes at 0.2C with respect to the normalized discharge − charge time.

scan rate of 0.1 mV s^{-1}. The CV profile of the MoSSe@graphene@CC cell in Fig. 3**a** displays two noticeable cathodic and two anodic peaks. The two noticeable cathodic peaks can be ascribed to the electrochemical reduction from S_8 to long-chain polysulfides (Li_2S_x, $4 \leq n \leq 8$) (at about 2.3 V) and the subsequent reduction from long-chain polysulfides to insoluble short-chain polysulfides Li_2S_2/Li_2S (at about 2.0 V). The two anodic peaks correspond to the oxidation from insoluble Li_2S_2/Li_2S to long-chain polysulfides Li_2S_x and long-chain polysulfides Li_2S_x to elemental S_8 [29]. However, only "one anodic peak" can be seen from the CV profile of the graphene@CC cell, suggesting sluggish redox kinetics. Compared with the graphene@CC electrode, the cathodic peak CII of the MoSSe@graphene@CC electrode shifts to higher potential while the anodic peaks of the MoSSe@graphene@CC electrode shift to lower potential, indicating that MoSSe can enhance the redox kinetics of soluble polysulfide and considerably reduce voltage polarization [30]. For instance, the voltage difference of the MoSSe@graphene@CC electrode (0.37 V) is much smaller than that of the counterpart (0.45 V), confirming the considerably reduced voltage polarization. In addition, the cell with the MoSSe@graphene@CC electrode present increased current intensity of both anodic and cathodic peaks due to the excellent polysulfide conversion capability, while the counterpart exhibits a broader anodic peak and decreased cathodic peaks along with a larger potential gap. The anodic peak current of the MoSSe@graphene@CC cell, which reaches a staggering 4.05 mA, compared to 3.31 mA for the graphene@CC cell.

Similarly, the cathodic peak current CII of the MoSSe@graphene@CC cell, a substantial 3.89 mA, is also markedly higher than that of the counterpart, which is a mere 2.91 mA. This difference in current values between the two cells suggests that the redox kinetics of the soluble polysulfide are dramatically enhanced for the MoSSe@graphene@CC cell. Moreover, the CV peak profiles of both the MoSSe@graphene@CC cell (Fig. S1**a**) and the graphene@CC cell (Fig. S1**b**) overlap well during the first three scans at a scan rate of 0.1 mV s^{-1}, implying the excellent electrochemical reversibility of both cells.

The Tafel plots, which provide valuable insight into the electrochemical behavior of materials, are deduced from the potentiostatic polarization measurements taken at the distinct peak position of the CV curve. These plots directly reflect the kinetic degree associated with the electrochemical process being studied [31]. The Li_2S oxidation reaction and the polysulfide reduction were investigated by potentiostatic polarization measurement as shown in Fig. S1**c-e**. The MoSSe@graphene@CC cell demonstrates a lower onset potential (Fig. S1**c**) and a higher current response for the Li_2S oxidation process than the control cell, implying the lower energy barrier of Li_2S decomposition [32].

Furthermore, the MoSSe@graphene@CC cell exhibits a higher onset potential (Fig. S1**d-e**) and a higher current for the polysulfide reduction than the graphene@CC cell, suggesting a lower energy barrier of polysulfide catalytic conversion. The Tafel plots (Fig. S1**f-h**) are fitted to obtain the slopes for investigating the electrocatalytic effect on the charge-transfer kinetics during the polysulfide conversion. The MoSSe@graphene@CC cell exhibits a smaller slope during the reduction and oxidation processes (Fig. S1**f-h**). The MoSSe@graphene@CC cell, in comparison to the graphene@CC cell, demonstrates a lower Tafel slope, registering at 42 mV dec^{-1} for peak A, 71 mV dec^{-1} for peak C I, and 45 mV dec^{-1} for peak C II, against the respective values of 69 mV dec^{-1} for peak A, 100 mV dec^{-1} for peak C I, and 77 mV dec^{-1} for peak C II for the graphene@CC cell. This marked reduction in the Tafel slope values, especially for the peaks A and C II, of the MoSSe@graphene@CC cell

provides conclusive evidence of an enhanced redox conversion rate.

The electrocatalytic effect of the MoSSe@graphene@CC was also investigated through a rigorous analysis of the onset potential of three distinct redox peaks. The baseline voltage and current density are defined as the value before the appearance of the redox peak, in which the variation in current density is at its smallest, mathematically expressed as dI/dV=0 [33]. In electrocatalysis, where numerous electrochemical phenomena are examined, the term 'onset potential' refers to a specific point on a graph where the current density is 10 μA cm^{-2} greater than the corresponding baseline current density.

It should be noted that the onset potential is different for cathodic and anodic peaks. Cathodic peaks' onset potential occurs when the current density is 10 μA cm^{-2} more negative than the baseline current density. Conversely, for anodic peaks, the onset potential occurs when the current density is 10 μA cm^{-2} more positive than the baseline current density [34]. This allows for a direct comparison between the MoSSe@graphene@CC and graphene@CC cathodes, as shown in Fig. 3**b-e** and Fig. S2**a-d** respectively. The MoSSe@graphene@CC peaks demonstrate a marked increase, reaching 2.471 V for site I and 2.097 V for site II. In contrast, the anodic onset potential drops to 1.974 V for site III, providing clear evidence that the MoSSe@graphene@CC cathode significantly accelerates the LiPSs redox kinetics due to its electrocatalytic effect. This effect is further corroborated by a comparison with the graphene@CC cathode, which exhibits cathodic onset potentials of 2.465 V for site I, 2.088 V for site II, and an anodic onset potential of 2.030 V for site III. Furthermore, the MoSSe@graphene@CC not only accelerates the redox reaction, but also noticeably reduces polarization within the cell, providing a dual advantage for improved cell performance [35].

The galvanostatic intermittent titration technique (GITT), a widely used analytical method in electrochemistry, was employed to assess polysulfide's internal resistance and redox kinetics. In particular, the MoSSe@graphene@CC cell, as depicted in Fig. 3**f-i**, stands out with its markedly lower polarization in both discharging and charging profiles. This is distinct from those of the graphene@CC cell, which exhibits higher polarization. To add further context, the polarization during the electrochemical operation was quantified using the internal resistance. This was achieved by applying equation, shown here:

$$\Delta R_{internal} = |V_{QOCV} - V_{CCV}|/I_{applied}$$

where $\Delta R_{internal}$ represents the internal resistance, V_{QOCV} is the quasi-open circuit voltage, V_{CCV} is the closed circuit voltage, and $I_{applied}$ is the current applied. Fig. 3**f-i** demonstrates that the MoSSe@graphene@CC cell exhibits a smaller internal resistance when compared to the graphene@CC cell. This is especially evident between the Li_2S nucleation and activation points, implying its superior electric conductivity relative to the graphene@CC cell.

To confirm the catalytic ability of the MoSSe@graphene@CC electrode, symmetrical cells with the red-brown Li_2S_6 catholyte were assembled. CV tests were then implemented at a scan rate of 0.5 mV s^{-1} within a voltage window ranging from −1.5 to + 1.5 V, as depicted in Fig. 4**a**. Upon analysis of the CV curves, two distinct reduction peaks emerged at potentials of −0.105 V and −0.434 V, while two prominent oxidation peaks located at + 0.105 V and + 0.434 V, respectively. Specifically, the anodic peaks at + 0.105 V (B peak) and + 0.434 V (C peak) are intimately linked to the electrochemical conversion of insoluble Li_2S_2/Li_2S to the more soluble LiPSs, followed by the oxidation from the long-chain LiPSs to S_8. In contrast, the two cathodic peaks at −0.105 V (D peak) and −0.434 V (A peak) are closely associated with the electrochemical reduction of S_8 to Li_2S_6, which is then followed by the subsequent reduction of Li_2S_6 to Li_2S [36]. However, for the graphene@CC electrode, it exhibits a pair of very broad redox peaks, which suggests that the electrochemical reduction of Li_2S_6 was considerably slow [37].

Furthermore, the MoSSe@graphene@CC symmetric cell demonstrates substantially higher redox response currents than the graphene@CC symmetric cell. This highlights the synergistic effect between the MoSSe nanosheets and graphene nanosheets, which can accelerate the redox reaction kinetics of soluble polysulfide species [38]. Moreover, Fig. 4**b** illustrates the detailed redox reaction mechanism occurring within the MoSSe@graphene@CC symmetric cell, elucidating the intricate interplay of various electrochemical processes.

To investigate and gain insights into the interfacial charge transfer resistance, EIS measurement was carried out within a frequency range (0.01 Hz-100 kHz) (Fig. 4**c-d**). Before cycling (Fig. 4**c**), an intercept on the real axis at high frequency associated with the electrolyte's internal resistance (R_e) can be easily observed from both Nyquist plots of two different cells. The Ohmic resistances for both cells share many similarities, suggesting a similar electrode and electrolyte environment. The charge-transfer resistance (R_{ct}), is represented by the single semicircle on the Nyquist plot. This resistance is directly related to the kinetics of the electrode reaction.

Meanwhile, the Warburg impedance (W_o), denoted by the inclined line, represents the Li-ion diffusion into the electrolyte. The constant phase elements (CPE2), on the other hand, represents the capacitance of the charge transfer process [39]. The fitted equivalent circuit was used to analyze the EIS data (Fig. 4**e**). As shown in Fig. 4**f**, it is noticed that the R_{ct} value of the MoSSe@graphene@CC cell (19.52 Ω) is smaller than that for the counterpart cell (63.64 Ω). This observation suggests that

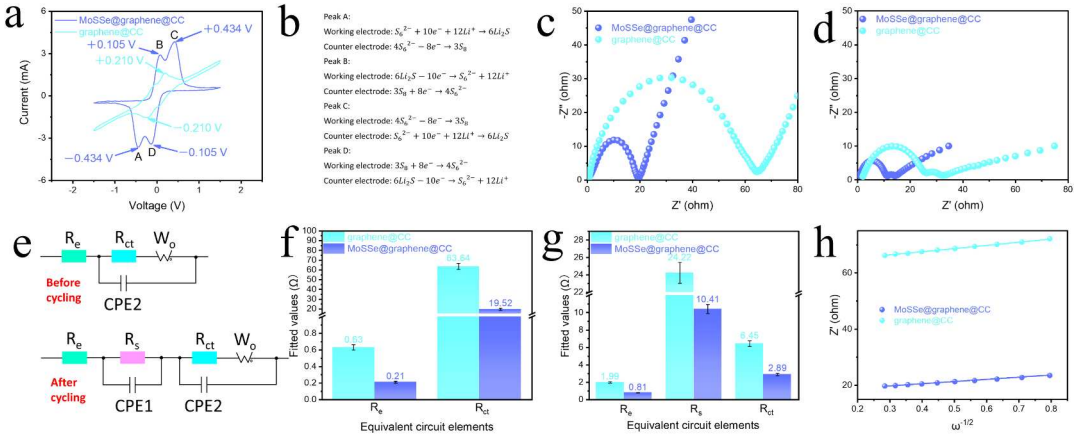

Fig. 4. (a) CV curves of the MoSSe@graphene@CC and the graphene@CC symmetric cells at 0.5 mV/s. (b) The corresponding chemical reactions for the redox peaks of the MoSSe@graphene@CC cell; Nyquist plots for the cells (c) before and (d) after cycling; (e) Equivalent circuit models before and after cycling; The fitted values for the equivalent circuit elements (f) before and (g) after cycling (the number of repeat experiments: 3); (h) Fitting curves of the Warburg resistance before cycling.

MoSSe nanosheets can possibly facilitate the charge transfer during the redox reactions, leading to improved active material utilization and a high delivered discharge capacity [40]. To identify any variations in charge transfer resistance, impedance test was also implemented and impedance data were also collected after cycling (Fig. 4**d**). For two different cells after cycling at 1C for 200 cycles (Fig. 4**d**), the internal electrolyte resistance (R_e) is represented by the real axis intercept at high frequency. In contrast, the semicircle from high to medium frequency indicates the internal resistance of the solid electrolyte interphase (SEI) film correlated with the insoluble Li_2S_2/Li_2S (R_s). The second semicircle at medium frequency denotes the charge transfer resistance (R_{ct}) [41]. For both cells, it is noted that two semicircles and a straight sloping line with a 45° angle at low frequency region. The Warburg impedance is denoted by the straight sloping line, representing the migration of Li^+ in the organic electrolyte [42]. The fitted equivalent circuit was used to interpret the EIS results (Fig. 4**e**). CPE1 is used to represent the capacitance of the electrode bulk in high-frequency region, CPE2 is associated with the capacitance of the charge transfer process at the interface between the sulfur and electrolyte. The semi-infinite Warburg diffusion impedance of the long-chain LiPSs is denoted by W_o [43]. The SEI film is the Li_2S layer formed on the electrode surface during discharge. It is well acknowledged that the electrochemical behavior of rechargeable Li-S batteries is greatly affected by two essential factors: R_{ct} and R_s. As anticipated (Fig. 4**g**), the MoSSe@graphene@CC cell shows a smaller R_{ct} value (2.89 Ω) and R_s value (10.41 Ω) than the graphene@CC cell (R_{ct} = 6.54 Ω and R_s = 24.22 Ω), which is primarily owing to its higher electrical conductivity during cycling [44]. The aforementioned EIS results verify that the MoSSe@graphene@CC cell has better electrochemical properties.

Additionally, the oblique is associated with Warburg impedance and the Li^+ diffusion coefficient DLi^+ is introduced to compare the diffusion kinetics, which can be calculated by the following equation [45].

$$D_{Li}{}^{+} = R^2T^2/2A^2n^4F^4C^2\sigma_\omega{}^2 \quad (1)$$

Where R is the gas constant (8.314 J $mol^{-1}K^{-1}$), T is the absolute temperature (298 K), A represents the surface area of the cathode (1.13 cm^2), n is the number of electrons per molecule during oxidation (here, n = 2), F represents Faraday's constant (96458 C mol^{-1}), C represents the concentration of lithium ions (1 M). Additionally, σ_ω is the Warburg impedance coefficient, which can be calculated by the following equation [46].

$$Z' = R_e + R_{ct} + \sigma_\omega\omega^{-1/2} \quad (2)$$

Where σ_ω is the angular frequency and $\omega = 2\pi f$ (*f* is the frequency). The σ_ω in Equation (2) is represented by the slope of the fitting line of Z' vs $\omega^{-0.5}$ (Fig. 4**h**), which is substituted into Equation (1) to obtain DLi^+. According to the calculation, the DLi^+ for the MoSSe@graphene@CC and graphene@CC cells are 3.20 × 10^{-17} and 1.29 × 10^{-17} cm^2s^{-1}, respectively. This result suggests a faster Li^+ diffusion in the MoSSe@graphene@CC cell, which is also confirmed by CV tests at various scan rates.

To further confirm the superiority of MoSSe@graphene@CC towards the electrochemical LiPSs conversion, Li_2S precipitation experiments were carried out. The conversion kinetics of LiPSs can be evaluated based on the distinctive ability of Li_2S deposited on the specific sulfur host materials. Consequently, the deposition capability of Li_2S was tested through potentiostatic discharge of the red-brown colored Li_2S_8 catholyte for two separate samples. For this test, the discharge cut-off voltage was set at 2.12 V, a value chosen specifically to consume large, substantial quantities of higher-order lithium polysulfides. It's generally understood that the nucleation and growth processes of Li_2S are highly dependent on the reactive interfaces of the specific sulfur host materials. Hence, Li_2S deposition tests on various surfaces were implemented to confirm the synergistic effect of MoSSe@graphene@CC hetero-structure. It is obvious that the MoSSe@graphene@CC cell demonstrates a higher precipitation capacity (323.7 mAh g^{-1}) suggesting a higher activity towards Li_2S precipitation (Fig. 5**a**) compared with the counterpart cell (184.6 mAh g^{-1}) (Fig. 5**b**). In additional, the responsivity of Li_2S nucleation of the MoSSe@graphene@CC cell was faster (1166 s) compared with the counterpart cell (4170 s). The results suggest that the MoSSe@graphene@CC cell can successfully enhance the adsorption capability towards LiPSs and facilitate the catalytic conversion of LiPSs and Li_2S.

To give further insight into the distinct Li_2S growth behaviors on both electrodes, a detailed analysis was conducted on the current–time response profiles. These profiles, obtained from potentiostatic electrodeposition tests, were fitted using a dimensionless current (I/I_m, I_m representing the maximum current) and time (t/t_m, t_m being the time to reach the maximum current) transient. This was done following four well-established classic electrochemical deposition models. Through applying theoretical formulas, as captured in the provided equations, it was possible to categorize the instantaneous (I) or progressive (P) nuclei formation. This categorization was based on whether it occurred through two-dimensional (2D) or three-dimensional (3D) growth direction modes, respectively [47].

Bewick, Fleischmann, and Thirsk (BET) models:

$$\frac{j}{j_m} = \left(\frac{t}{t_m}\right)^2 exp\left[-\frac{2}{3}\left(\frac{t^3 - {t_m}^3}{{t_m}^3}\right)\right] \quad \text{for 2DP}$$

$$\frac{j}{j_m} = \left(\frac{t}{t_m}\right) exp\left[-\frac{1}{2}\left(\frac{t^2 - {t_m}^2}{{t_m}^2}\right)\right] \quad \text{for 2DI}$$

Scharifker-Hills (SH) models:

$$\left(\frac{j}{j_m}\right)^2 = \frac{1.2254}{t/t_m}\left[1 - exp\left(-2.3367\frac{t^2}{{t_m}^2}\right)\right]^2 \quad \text{for 3DP}$$

$$\left(\frac{j}{j_m}\right)^2 = \frac{1.9542}{t/t_m}\left[1 - exp\left(-1.2564\frac{t}{t_m}\right)\right]^2 \quad \text{for 3DI}$$

The set of mathematical models developed by Bewick, Fleischman, and Thirsk, which are referred to as the BFT models, are specifically designed to delineate two-dimensional (2D) progressive (2DP) or instantaneous (2DI) nucleation. Following the nucleation stage, these models track the subsequent growth process, during which adatoms become incorporated into the crystalline lattice structure. In contrast, the Scharifker–Hills (SH) models are used to elucidate three-dimensional (3D) progressive (3DP) or instantaneous (3DI) nucleation. These models conceptualize the evolving 3D structure as a hemispherical nucleus. This nucleus is envisioned to grow under the influence of ion diffusion, a process that is intrinsically controlled by the system's characteristics [48]. Both the BFT and SH models are articulated in mathematical language, capturing the intricate dynamics of the phenomena. These two sets of models and their underlying mathematical formulations are illustrated in the figures, offering a comprehensive visual representation of the four classic electrochemical deposition patterns (**Fig. S3**).

Potentiostatic discharge profiles were analyzed and fitted with four theoretical deposition models, as illustrated in Fig. 5**c-d**. The MoSSe@graphene@CC electrode shows 3DP Li_2S nucleation, implying that Li_2S growth is associated with fast ion diffusion [49]. The Li_2S precipitation behavior could be profoundly influenced and regulated by two key factors: surface lateral atomic diffusion and mass transport in the electrolyte [50]. Consequently, the 3DP Li_2S growth mode of the MoSSe@graphene@CC electrode suggests that the growth rate is primarily regulated by ion diffusion. This phenomenon can be attributed to the facilitated fast ion diffusion on the surface of the MoSSe@graphene@CC electrode [51]. This suggests the surface active sites of the MoSSe@graphene@CC electrode could successfully manipulate the radical Li_2S growth, and the surface passivation issue can be effectively avoided [52]. However, when using the graphene@CC electrode, Li_2S growth

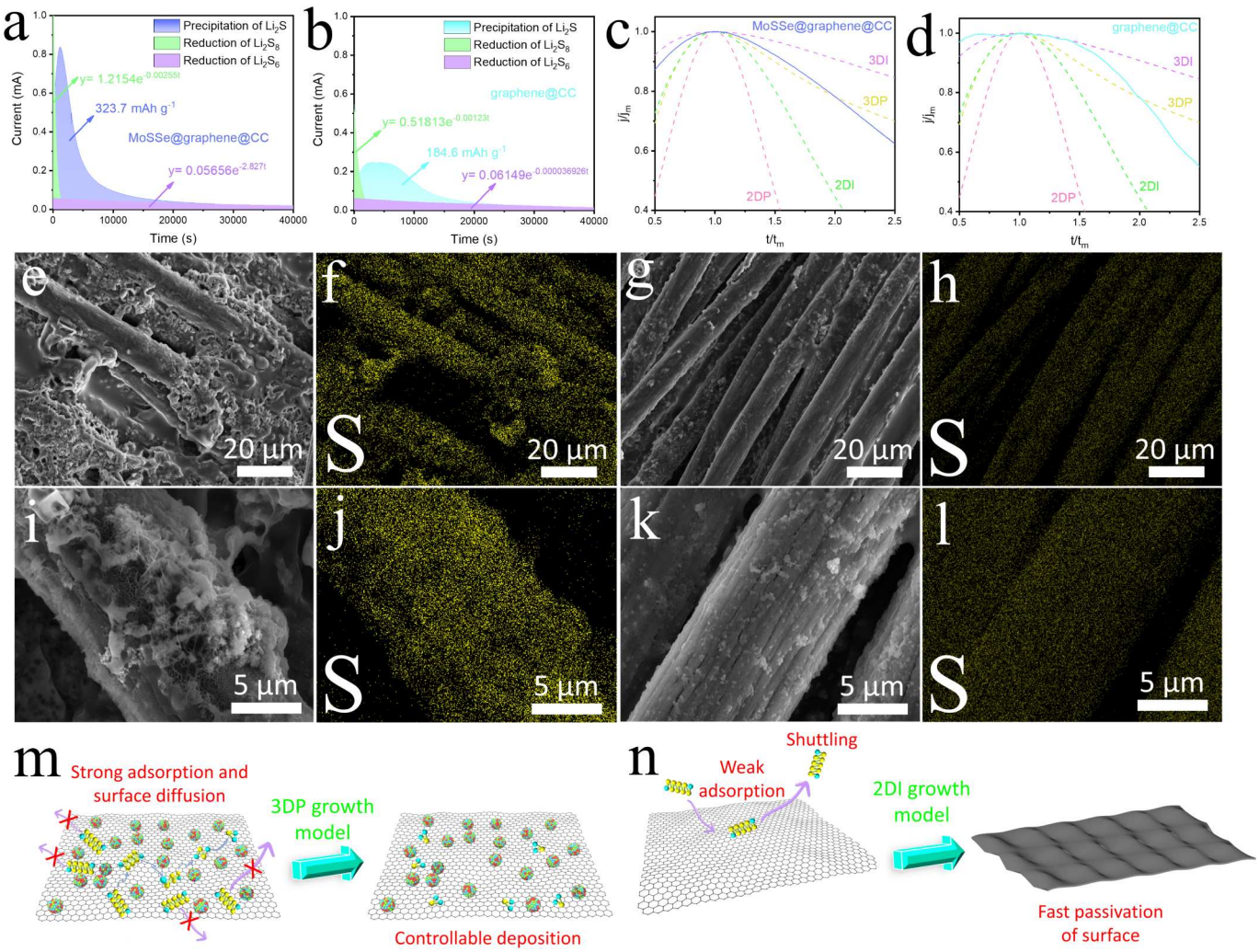

Fig. 5. Potentiostatic discharge curves of Li_2S_8 on the (a) MoSSe@graphene@CC and (b) graphene@CC samples. Dimensionless transient current–time profiles of Li_2S deposition on the (c) MoSSe@graphene@CC and (d) graphene@CC samples. The dash lines represent the simulated results from the theoretical 2D and 3D models. SEM images and EDS sulfur mappings analysis after the $Li_2S_{1/2}$ deposition on MoSSe@graphene@CC (e-f and i-j), and graphene@CC (g-h and k-l). Schematic illustration of the Li_2S deposition and growth process on (m) MoSSe@graphene@CC and (n) graphene@CC surfaces.

shows a tendency to the 2DI model, leading to the formation of Li_2S nucleation, which made its surface easily passivated [53].

Next, the cycled cells were disassembled and subjected to SEM imaging. The surfaces of both cathodes (the MoSSe@graphene@CC cathode and the graphene@CC cathode) were analyzed after the Li_2S precipitation test. Thicker and rougher Li_2S deposition formed on the surface of the MoSSe@graphene@CC cathode (Fig. 5**e,i**), which is consistent with the higher deposition capacity. Li_2S deposits not just in a thin film mode but in a 3D morphology on the surface of the MoSSe@graphene@CC cathode (Fig. 5**e,i**). This deposition pattern is consistent with the 3DP nucleation model discussed previously, where Li_2S nucleates and grows in a 3D manner on the cathode surface. However, small Li_2S particles are distributed nonuniformly on the surface of the graphene@CC cathode and the graphene@CC cathode surface is heavily passivated by thin Li_2S films (Fig. 5**g,k**), which are caused by the less dominant nucleation sites. The EDS mappings of the sulfur element also demonstrate that more Li_2S deposits on the MoSSe@graphene@CC cathode surface (Fig. 5**f,j**) than on the graphene@CC cathode surface (Fig. 5**h,l**), further confirming the enhanced Li_2S deposition by the hetero-structure of the MoSSe@graphene composite. Considering that the same solvent was used, the huge difference in deposition morphology on both cathode surfaces can be attributed to the embedded MoSSe nanosheets with high electrochemical activity [54]. The MoSSe nanosheets functioning as active sites guide selective nucleation and growth, mitigating surface passivation (Fig. 5**m-n**). Additionally, more Li_2S originating from the disproportionation reaction of LiPSs has a strong tendency to precipitate on the pre-formed Li_2S particles owing to the strong chemical interaction among analogous species, which is important to fulfill the 3D morphology and a larger Li_2S deposition capacity. The strong chemical interaction between the MoSSe nanosheets and LiPSs significantly weakens the Li–S bonds, decreasing the energy barrier of the LiPS electrochemical reduction process. The oxidation of deposited lithium sulfide (Li_2S) is analyzed via a potentiostatic charging process, as illustrated in Fig. S4**a-b**. Analogically, the dissolution capacity of MoSSe@graphene@CC is significantly higher compared to graphene@CC, implying that MoSSe@graphene@CC dramatically expedites the solid-to-liquid conversion of Li_2S into lithium polysulfides. The comprehensive results validate that the MoSSe@graphene@CC exhibits exceptional catalytic potential concerning the precipitation and dissolution of Li_2S.

The Li-ion diffusion ability was assessed by CV measurement at various scan rates (Fig. 6**a-b**) [55–57]. At the same scan rate, the MoSSe@graphene@CC cell demonstrates higher cathodic peak currents (I_{C1}, I_{C2}) and anodic peak current (I_A) than the graphene@CC cell (Fig. S5**a-c**). Fig. 6**c-e** displays the connection of cathodic peak currents (I_{C1}, I_{C2}) and anodic peak current (I_A) with the square root of the scan

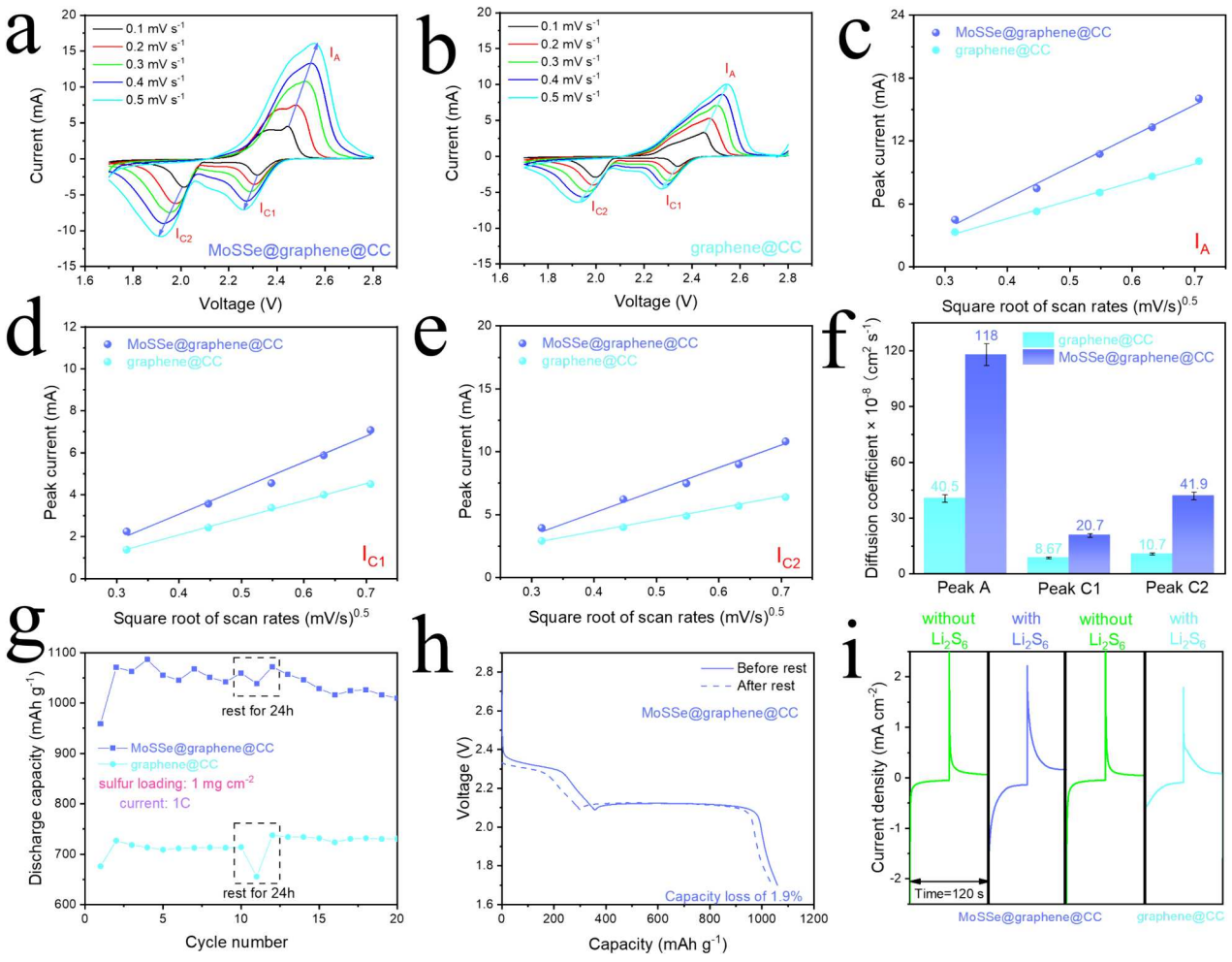

Fig. 6. CV curves of Li–S cells with (a) MoSSe@graghene@CC and (b) graphene@CC electrodes at various scan rates; (c-e) plots of peak current vs square root of scan rates for the peaks A, C1, and C2. (f) A columnar comparison of the diffusion coefficients of three peaks for the MoSSe@graghene@CC and the graphene@CC cells (the number of repeat experiments: 3). (g) Self-discharge cycling performance at 1C. (h) Comparison of discharge curves before and after 24 h rest of MoSSe@-graphene@CC cell. (i) Chronoamperometric curves of Li_2S_6 symmetric cells.

rates. It is also worth noting that the slopes of cathodic peak currents (I_{C1}, I_{C2}) and anodic peak current (I_A) of the MoSSe@graphene@CC cell in the cathodic scan and anodic scan process are higher than those of the counterpart cell (Fig. 6**c-e**), implying that the favorable hetero-structure of MoSSe anchored on conductive graphene sheets achieves accelerated Li ion diffusion rate.

Additionally, the classic Randles–Sevcik equation below was used to calculate the Li-ion diffusion coefficient and evaluate Li-ion diffusion dynamics.

$$I_p = \left[2.69 \times 10^5 A n^{1.5} D_{Li^+}^{0.5} C_{Li^+}\right] \upsilon^{0.5}$$

Where I_p indicates the peak current of redox peak in amperes (A), n is the number of transferred electrons in reaction (for Li-S batteries, n = 2), A represents the effective area of the electrode (here, A=1.13 cm^2), C_{Li+} is the concentration of Li-ion in the electrolyte (here, C_{Li+} = 0.001 mol cm^{-3}), D_{Li+} is the coefficient of Li ion diffusion and ν is the adjustable scan rate (V s^{-1}) [58]. Lithium-ion diffusion coefficient (D_{Li+}) is a crucial parameter for evaluating redox kinetics. Since n, A, and C_{Li+} are constant, the square root of the diffusion coefficient $(D_{Li+})^{0.5}$ is proportional to the slope $I_p/\nu^{0.5}$ Fig. 6**f** exhibits a column graph quantifying the Li-ion diffusion coefficient calculated based on the slopes ($i_p/\nu^{0.5}$). The latter sample has a higher diffusion coefficient when comparing the diffusion coefficients at all redox peaks. The higher Li-ion transfer rate guarantees the smooth conversion of polysulfide intermediates and further mitigates the surface passivation of the electrode [59]. This further validates that the MoSSe nanosheet is an efficient catalyst to achieve the accelerated conversion of soluble polysulfides and enhanced redox kinetics.

The severe self-discharge behavior is another major limitation of Li-S batteries, mainly caused by the shuttle effect [60–62]. As illustrated in Fig. 6**g**, Li-S cells were assembled with either a graphene@CC electrode or a MoSSe@graphene@CC electrode. Initially, they were galvanostatically discharged and charged at 1C for ten consecutive cycles. Subsequently, the cells were allowed to rest for 24 h before the 11th cycle, also at 1C. In the case of the battery incorporating the graphene@CC electrode (**Fig. S6**), approximately 8.2 % of its capacity was lost over the 24-hour rest period. This capacity loss was evident from the discharge curves presented in **Fig. S6**. Conversely, for the battery incorporating the MoSSe@graphene@CC electrode (Fig. 6**h**), there was no discernible decrease in either capacity or discharge plateau voltage. This evidence suggests that the MoSSe@graphene@CC electrode significantly mitigates the shuttle effect in Li-S batteries, thereby suppressing capacity fade. In Fig. 6**i**, the chronoamperometry curves of symmetric cells incorporating Li_2S_6 display an enhanced current response compared to cells lacking Li_2S_6. This observation suggests that the current responses are predominantly influenced by the lithiation-delithiation reaction pathway rather than the double-layer capacitance [63]. Moreover, the MoSSe@graphene@CC electrode exhibits a higher current response, which proves its improved LiPS affinity and enhanced redox kinetics.

Fig. 7**a** displays the 1st discharge/charge curves of both cells at 0.2C. It is noted that the discharge/charge profiles display two observable reduction plateaus. The upper discharge plateau corresponds to the electrochemical conversion of S_8 to soluble long-chain polysulfides [64]. The lower discharge plateau is related to the electrochemical transformation of the soluble long-chain polysulfides to insoluble Li_2S_2/Li_2S, the main delivery of discharge capacity in the Li-S cells [65]. The initial discharge capacities are 1305 mAh g^{-1} and 973 mAh g^{-1}, respectively. The lower discharge plateau, which was greatly extended with the aid of MoSSe nanosheets, substantiates that the MoSSe@graphene@CC cell accelerates the reaction kinetics of the electrochemical conversion of polysulfides to the final discharge product Li_2S_2/Li_2S and demonstrates superb electrochemical behavior. Fig. 7**b-c** exhibits a distinct valley between the high and low discharge plateau. This valley is referred to as the "nucleation point", a particularly notable feature [66]. The potential difference exists between the tangential of the low discharge plateau and the nucleation point. This difference was employed to evaluate the redox kinetics associated with Li_2S nucleation. A comparison reveals a disparity in their respective nucleation overpotentials. Specifically, the MoSSe@graphene@CC cell demonstrates a reduced nucleation overpotential of merely 18 mV, significantly lower than the 22 mV observed in the counterpart cell. Moreover, the ratio of Q_2/Q_1 is often utilized as a means of assessing the catalytic activity of the sulfur host materials throughout their cycling lifespan. In this context, Q_1 and Q_2 serve to designate the respective capacities of the two distinct discharge plateaus, elucidated in Fig. 7**d-e**. In light of the electrons involved in two different processes (for Q_1, $S_8 + 4Li^+ + 4e^- \rightarrow 2Li_2S_4$ and for Q_2, $2Li_2S_4 + 12Li^+ + 12e^- \rightarrow 8Li_2S$), the calculated capacity ratio should be $Q_2/Q_1 = 3$ under ideal conditions [67]. However, the calculated Q_2/Q_1 ratio in reality is generally lower than 3 due to the sluggish redox kinetics of LiPSs and the huge loss of active materials caused by the polysulfide shuttling. Importantly, the MoSSe@graphene@CC cell demonstrates a higher Q_2/Q_1 ratio of 2.62 (Fig. 7**e**), which is attributed to its accelerated redox kinetics and the effective inhibition of soluble LiPSs. Moreover, a lower electrode polarization voltage (ΔE) was also observed for the MoSSe@graphene@CC cell (221 mV). These results suggest that the MoSSe@graphene@CC cell successfully reduces the overpotential of the electrochemical reaction and fulfills bidirectional catalysis for sulfur species. Next, long-term cycling performance tests were carried out (Fig. 7**f**). As expected, the MoSSe@graphene@CC demonstrates superb cycling performance compared to the counterpart. After 100 cycles at 0.2 C, the MoSSe@graphene@CC cell remains as high as 1287 mAh g^{-1}, corresponding to a minimal capacity fading rate of 0.014 % per cycle. However, for the battery with the @graphene@CC electrode, the observed discharge capacity is only 903 mAh g^{-1} after 100 cycles at 0.2 C, suggesting a serious capacity decay rate of 0.072 % per cycle. The charge/discharge curves at different rates for the MoSSe@graphene@CC cell are exhibited in Fig. 7**g**. The charge/discharge voltage plateaus rise/drop as the current density increases. The two representative discharge plateaus are still noticeable, and the charge plateau is also observable. An initial specific capacity of 1305 mAh g^{-1} was obtained by the MoSSe@graphene@CC cell at 0.2C (1C=1675 mA g^{-1}). Along with the increase of the current rate to 0.5, 1, 2, 3, and 5C, an outstanding initial specific capacity of 1182, 1091, 998, 878, and 678 mAh g^{-1} were obtained at various current densities, respectively. The corresponding sulfur utilization rates of the MoSSe@graphene@CC cell at 0.2, 0.5, 1, 2, 3, and 5C are 77.9 %, 70.6 %, 65.1 %, 59.6 %, 52.4 %, and 40.5 %, respectively (Fig. 7**h**). The long cycling performances at 1C are shown in Fig. 7**i**. It is noticed that the MoSSe@graphene@CC cell can be cycled up to 1000 cycles. The specific discharge capacity slowly decreases from 1091 mAh g^{-1} at the 1st cycle to the final capacity of 656 mAh g^{-1} at the 1000th cycle, corresponding to a minimal capacity degradation rate of 0.040 % per cycle. However, the graphene@CC cell exhibits a lower initial discharge capacity of 760 mAh g^{-1} and a noticeable capacity drop between 302 and 358 cycles. Moreover, the graphene@CC cell fails at the 358th cycle with a final discharge capacity of 405 mAh g^{-1}, implying a severe capacity attenuation rate of 0.130 % per cycle and testifying to a severe active sulfur loss. Such an inferior

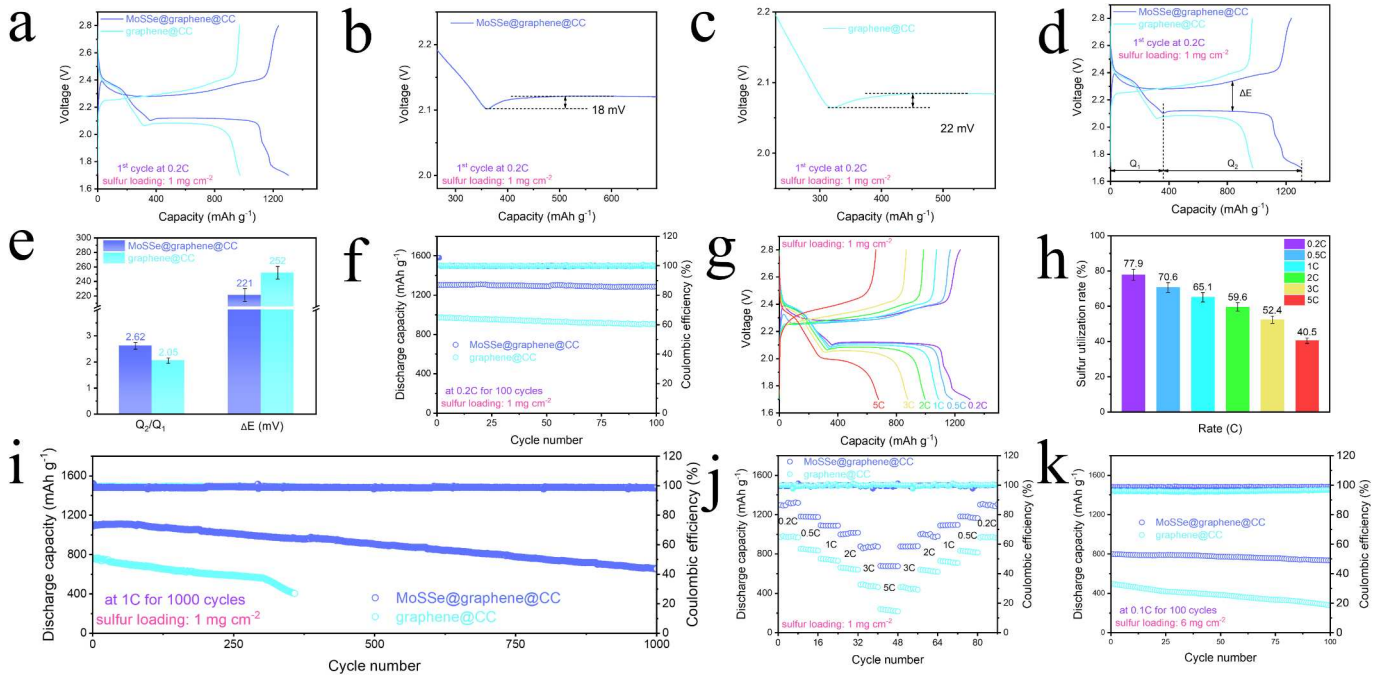

Fig. 7. (a) Charge–discharge curves at 0.2C for the 1st cycle; The overpotential of Li_2S nucleation of the cells with (b) MoSSe@graphene@CC and (c) graphene@CC electrodes. (e) ΔE and Q_2/Q_1 values (the number of repeat experiments: 3) obtained from (d) the charge–discharge profiles of the cells with MoSSe@graphen@CC, and graphene@CC electrodes at 0.2C. (f) Cycling performance at 0.2C for 100 cycles of the MoSSe@graphene@CC and the graphene@CC cells. (g) Charge–discharge curves at different C-rates and (h) the corresponding sulfur utilization rates at different C-rates of the MoSSe@graphene@CC cell (the number of repeat experiments: 3). (i) Cycling performance at 1C, (j) rate performances, and (k) cycling performance at 0.1C for 100 cycles under high sulfur loading (6 mg cm^{-2}) of the MoSSe@graphene@CC and the graphene@CC cells.

electrochemical performance is attributed to the fact that the non-polar graphene, without the help of the polar MoSSe nanosheets, can only provide limited physical confinement against polysulfide migration. Testing of the rate performances further demonstrates the superior electrochemical behavior of the MoSSe@graphene@CC cell (Fig. 7**j**). At 0.2C rate, the MoSSe@graphene@CC cell delivers a higher initial discharge capacity of 1298 mAh g^{-1} than the graphene@CC cell which only reaches 972 mAh g^{-1} for the 1st cycle at 0.2C (Fig. 7**j**). With the increase in the current density, the MoSSe@graphene@CC cell exhibits the discharge capacities of 1181, 1091, 999, 878 and 679 mAh g^{-1} at 0.5, 1, 2, 3 and 5C, respectively. The discharge capacity of the MoSSe@graphene@CC cell restores to 1301 mAh g^{-1} when the current density returns to 0.2C, demonstrating a superb capacity retention capability (Fig. 7**j**). In comparison to the MoSSe@graphene@CC cell, the discharge capacity of the graphene@CC cell decreases from 972 mAh g^{-1} to 239 mAh g^{-1} after undergoing a current density ranging from 0.2 to 5C. When the current density finally reverts to 0.2C, the graphene@CC cell delivers a much lower capacity of 967 mAh g^{-1}, implying an inferior rate performance with varied current densities. Overall, the MoSSe@graphene@CC cell exhibits its superiority in rate performance and cycling stability. The favorable electrochemical characteristics of the assembled Li-S cells with the MoSSe@graphene@CC electrode are attributed to the incorporation of MoSSe anchored on graphene architecture. The hereto-structure engineering of MoSSe with intrinsic polar characteristics and graphene with a large surface area restricts the polysulfide migration by chemical adsorption instead of mere physical confinement [68]. Additionally, MoSSe demonstrates the promising electrocatalytic capability of the electrochemical conversion of long-chain intermediate polysulfides to lower-order polysulfides, accelerating the electrochemical conversion in both discharge and charge stages and ultimately fulfilling the improvement of active material sulfur utilization. To allow the energy density of Li-S batteries comparable to that of commercial Li-ion batteries and enhance the commercial viability of the Li–S batteries, the Li-S batteries were assembled with a high sulfur loading of 6 mg cm^{-2}. The cycling profiles under a high sulfur loading of 6 mg cm^{-2} at 0.1C are exhibited in Fig. 7**k**. As shown in Fig. 7**k**, the MoSSe@graphene@CC cell delivers a high initial capacity of 799 mAh g^{-1} and a discharge capacity of 734 mAh g^{-1} can be maintained after 100 cycles at 0.1C with a high sulfur loading of 6 mg cm^{-2}, corresponding to a minimal capacity attenuation rate of 0.081 % per cycle. However, the graphene@CC cell presents an unsatisfactory initial capacity of 497 mAh g^{-1} and a reversible discharge capacity of 278 mAh g^{-1} after 100 cycles, implying a formidable capacity decay rate of 0.441 % per cycle. This can be attributed to the fast redox reaction and conversion of the polysulfides on the MoSSe nanosheets, achieving a favorable sulfur utilization rate and successful inhibition of the polysulfide shuttling.

It is worth mentioning that Li_2S nucleation and decomposition are recognized as the "rate-determining" steps during sulfur redox reactions due to the sluggish "liquid ↔ solid" transformation and the insulating characteristic of Li_2S [69]. To gain insight into the enhanced effect of MoSSe@graphene composite on dual-directional electrocatalysis, potentiostatic intermittent titration technique (PITT) was used to demonstrate the quantitative analysis. Regarding Li_2S precipitation, the assembled coin cells were potentiostatically discharged from 2.25 to 1.90 V at 50.0 mV intervals and 3600 s holding period per interval. As for the Li_2S oxidation, the assembled coin cells were potentiostatically charged from 2.20 V to 2.45 V using the same parameters. Generally, the PITT discharge curves of Li_2S_8 catholyte can be divided into two regions [70]. The first region is the liquid–liquid electrochemical conversion. The current plunges and reaches stability between 2.25 and 2.10 V, corresponding to the electrochemical conversion from long-chain polysulfides to short-chain polysulfides. The second region is the liquid–solid electrochemical conversion. At the constant voltage platform of 2.05 V, the current responses show a bump (Fig. 8**a-b**), suggesting that Li_2S nucleation occurs for both cells. The nucleation peak of Li_2S is significantly earlier (261 min) for the MoSSe@graphene@CC cell compared with the counterpart(274 min), implying that the redox kinetics of the liquid–solid electrochemical conversion is fast on the MoSSe@graphene@CC cell (Fig. 8**c**). The nucleation/dissociation capacity of lithium sulfide (Li_2S) can be determined by a methodical integration of the current density over time at the voltage corresponding to the peak currents. The nucleation capacities on both cathodes are 331 and 207 mAh g^{-1} (Fig. 8**d**), respectively. Through the entire discharge PITT, the MoSSe@graphene@CC cell displays a superior discharge capacity of 331 mAh g^{-1}, which was 1.6 times than that of the graphene@CC cell (Fig. 8**d**). Similarly, the oxidation of Li_2S for the MoSSe@graphene@CC cell occurs at a lower potential in contrast to the counterpart. For the MoSSe@graphene@CC cell, the dissolution of Li_2S began at 2.25 V with an obvious current peak observed to indicate phase transition (Fig. 8**e**). However, the graphene@CC cell demonstrates a current peak at 2.30 V (Fig. 8**f**). The collected peak response time and calculated nucleation capacity of the MoSSe@graphene@CC cell are superior (Fig. 8**g-h**). It delivers a shorter response time (103 min) and a larger dissolution capacity (372 mAh g^{-1}) than the counterpart (130 min and 220 mAh g^{-1}). Through the entire charge PITT, the MoSSe@graphene@CC cell exhibits an excellent charge capacity of 372 mAh g^{-1}, 69 % higher than that of the graphene@CC cell (Fig. 8**h**). Therefore, the participation of the MoSSe nanosheets considerably improved the electrochemical conversion kinetics for both Li_2S deposition and

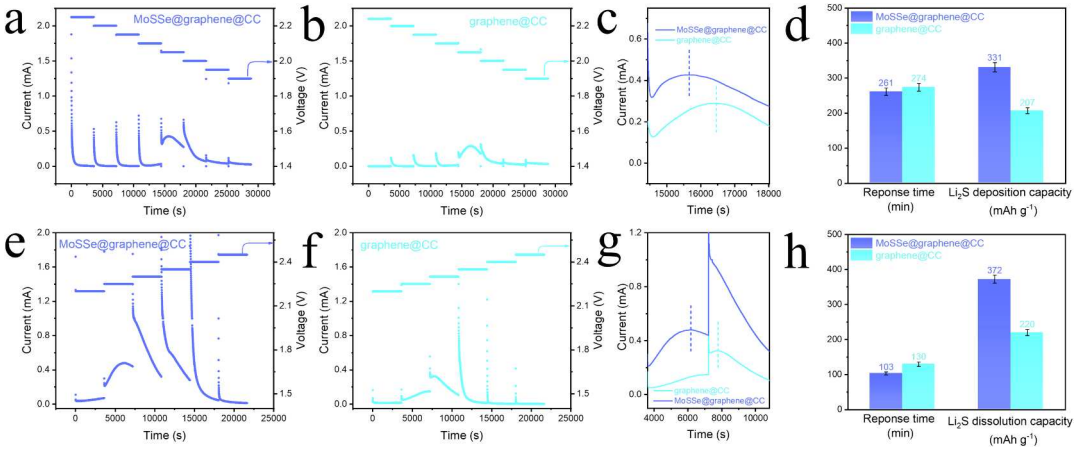

Fig. 8. (a-c) Current profiles and (d) corresponding response time coupled with calculated Li_2S deposition capacity, under the discharging PITT operation of Li_2S_8 half-cells with MoSSe@graphene@CC, and graphene@CC (the number of repeat experiments: 3). (e-g) Current profiles and (h) corresponding response time coupled with calculated Li_2S dissolution capacity under the charging PITT operation of the two half-cells (the number of repeat experiments: 3).

dissolution and significantly enhanced the capacity of both processes [71].

The soluble polysulfides, generated at the cathode during the discharge phase of the battery, can diffuse across to the Li anode side. Here, they undergo a reduction process leading to the formation of insoluble Li_2S_2 and Li_2S. This particular reaction contributes significantly to an irreversible capacity loss in the battery, a critical issue that needs to be addressed. The phenomenon, commonly referred to as the "shuttle effect," can be readily observed and quantified by analyzing the shuttle current, as depicted in Fig. 9**a** [66]. Upon a comprehensive evaluation, the shuttle current of the MoSSe@graphene@CC cell was found to be approximately $\approx 1.05 \times 10^{-2}$ mA cm^{-2}. This value is remarkably lower than the shuttle current recorded for the graphene@CC cell, which stood at 3.36×10^{-2} mA cm^{-2}. This difference indicates that the MoSSe@graphene@CC electrode demonstrates superior efficacy in trapping polysulfides and mitigating the harmful effects of the shuttle effect [72].

A visualized polysulfide adsorption experiment was then carried out to evaluate the adsorption capability of MoSSe@graphene composite and graphene as exhibited in the inset of Fig. 9**b**. The Li_2S_6 catholyte mixed with MoSSe@graphene composite exhibits the decoloration after 2 h adsorption test compared with the Li_2S_6 solution mixed with graphene, implying a strong trapping capability towards polysulfide. However, the Li_2S_6 solution with graphene remained yellow. In addition, ultraviolet/visible absorption spectroscopy was implemented to determine residual polysulfides in two electrolyte samples. An absorption band attributed to Li_2S_6 at about 250–300 nm becomes weaker after adding MoSSe@graphene composite. This observation serves as powerful evidence and further confirms the impressive adsorption capability of the MoSSe@graphene composite [73].

The MoSSe@graphene powder, after being thoroughly soaked in the Li_2S_6 catholyte solution, was then put under rigorous analysis using XPS. The main objective of this analysis was to study and understand the complex chemical interactions that might occur between the

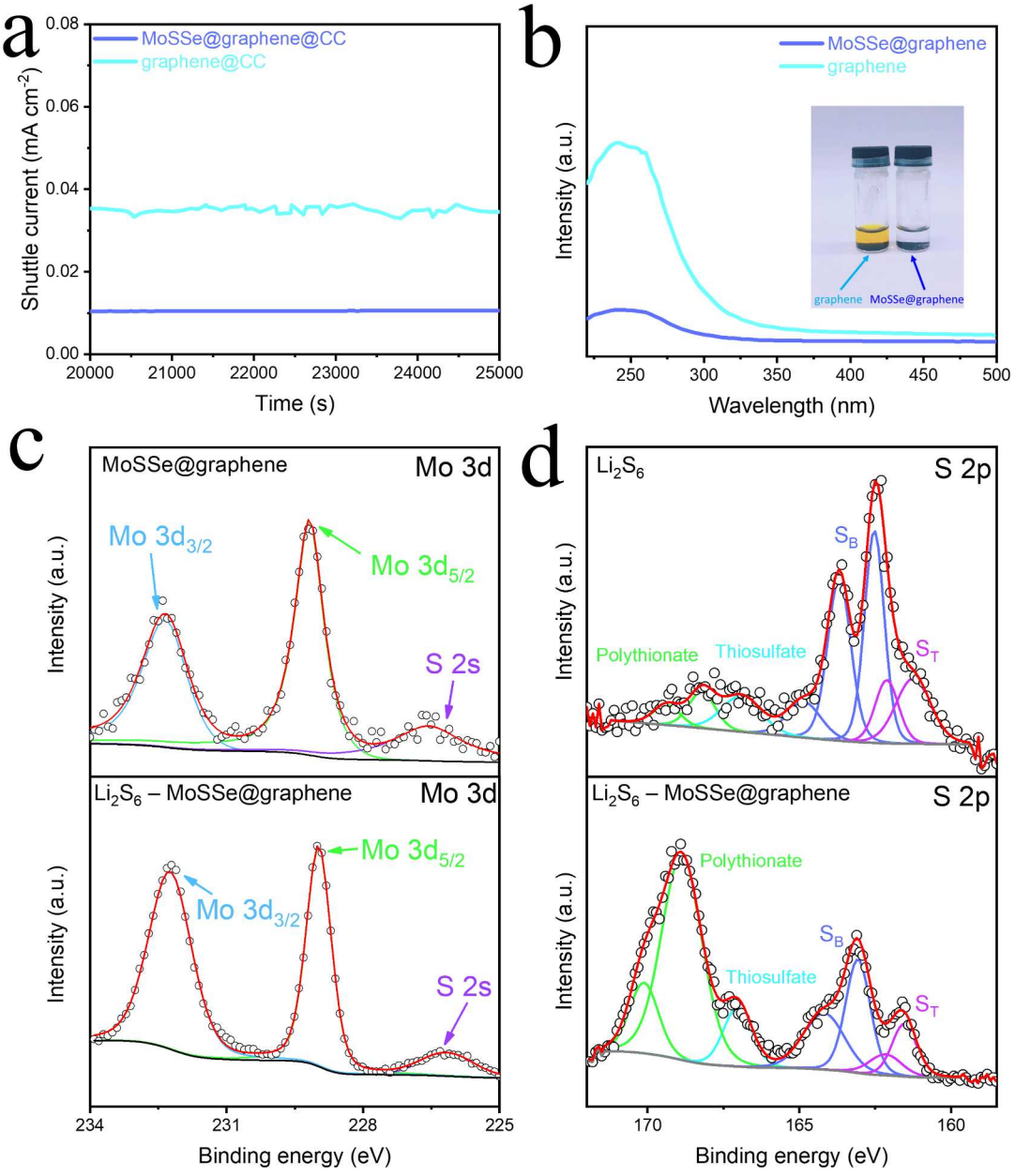

Fig. 9. (a) Shuttle currents of Li–S batteries without $LiNO_3$ additive. (b) UV–vis adsorption spectra of Li_2S_6 with graphene and MoSSe@graphene. The inset shows the corresponding Li_2S_6 adsorption test. High-resolution XPS spectra of (c) Mo 3d and (d) S 2p before and after the Li_2S_6 adsorption test.

MoSSe@graphene and Li_2S_6. As depicted in Fig. 9**c**, in comparison to the Mo 3d spectrum of the pristine MoSSe@graphene powder, a notable observation is that the distinctive Mo 3d peaks exhibit a discernible shift towards a lower binding energy post Li_2S_6 adsorption. Moreover, the S 2p peaks corresponding to the Li_2S_6 polysulfides which were adsorbed within the MoSSe@graphene composite demonstrate a prominently observable shift to a higher binding energy, as depicted in Fig. 9**d**. Such substantial peak shifts provide a clear indication of the deviation of electrons away from the highly electronegative S atoms and towards the more electropositive Mo atoms. This electron movement results in the formation of a charge shielding effect [74]. As illustrated in Fig. 9**d**, the pristine Li_2S_6 exhibits two prominent S $2p_{3/2}$ peaks at 161.2 and 162.5 eV, which are attributed to the bridging (S_T) and terminal (S_B) sulfur atoms, respectively. When contacted with the MoSSe@graphene composite, these peaks experience a noticeable shift to higher binding energies: 161.6 and 163.1 eV for the S $2p_{3/2}$ resonances. Such a positive shift is closely correlated with a reduction in the electron density along the sulfur chain. This phenomenon is a direct consequence of the chemical interaction between the Li_2S_6 and the MoSSe [75].

Furthermore, distinct peaks become evident at higher energy levels (167.1 eV for S 2p), a phenomenon that can be attributed to the formation of thiosulfate groups. The subsequent interaction of LiPSs with the firmly anchored thiosulfate groups is directly responsible for the emergence of a polythionate peak, discernible at a binding energy of 168.9 eV. This polythionate peak is a direct result of a complex redox reaction between Li_2S_6 and MoSSe, mediated through the formation of thiosulfate [76]. Utilizing XPS analysis, it becomes evident that the MoSSe@graphene sulfur host primarily relies upon the formation of chemical bonding to accomplish the process of chemical adsorption. The utilization of chemical bonding for adsorption purposes leads to a significant attenuation of the polysulfide shuttling effect, thereby enhancing the overall stability and efficiency.

3.3. Microscopic characterizations after cycling

Moreover, the batteries were disassembled after 200 cycles at 1C to study the polysulfide adsorption capability and the polysulfide conversion ability of MoSSe during the cycling process. After cycling (Fig. 10**a, e**), the slight color change of the separator in the MoSSe@graphene@CC cell was found, suggesting the efficient restriction of polysulfide dissolution by MoSSe. Furthermore, minor corrosion can be detected on the surface of Li metal anode paired with the MoSSe@graphene@CC cathode implying outstanding polysulfide adsorption capability and superb polysulfide conversion ability of MoSSe towards soluble long-chain LiPS (Fig. 10**b,f**).

Moreover, to investigate the polysulfide-blocking capabilities, the cycled Li metal anodes were characterized by SEM. The Li metal anode assembled with the graphene@CC electrode has an uneven, rough surface with a crack structure, implying inhomogeneous Li^+ deposition and corrosion induced by the polysulfide shuttling (Fig. 10**c-d**). Contrastively, the Li metal anode assembled with the MoSSe@graphene@CC cathode demonstrates a much smoother and more compact surface, suggesting the successful inhibition of the polysulfide migration (Fig. 10**g-h**). The enhanced lithium deposition state is attributed to the effective regulation of Li-ion deposition and mitigation of polysulfide corrosion to the lithium anode. The element mappings, as illustrated in Fig. 10**i-k and 10m-o**, provide additional confirmation of the mitigated shuttling issue. This is evidenced by a discernibly weaker signal of the sulfur element, probed within the cycled lithium anode of the MoSSe@graphene@CC cell. A gold coating was applied to both cycled lithium anodes to enhance conductivity and alleviate the buildup of electrons on the surface.

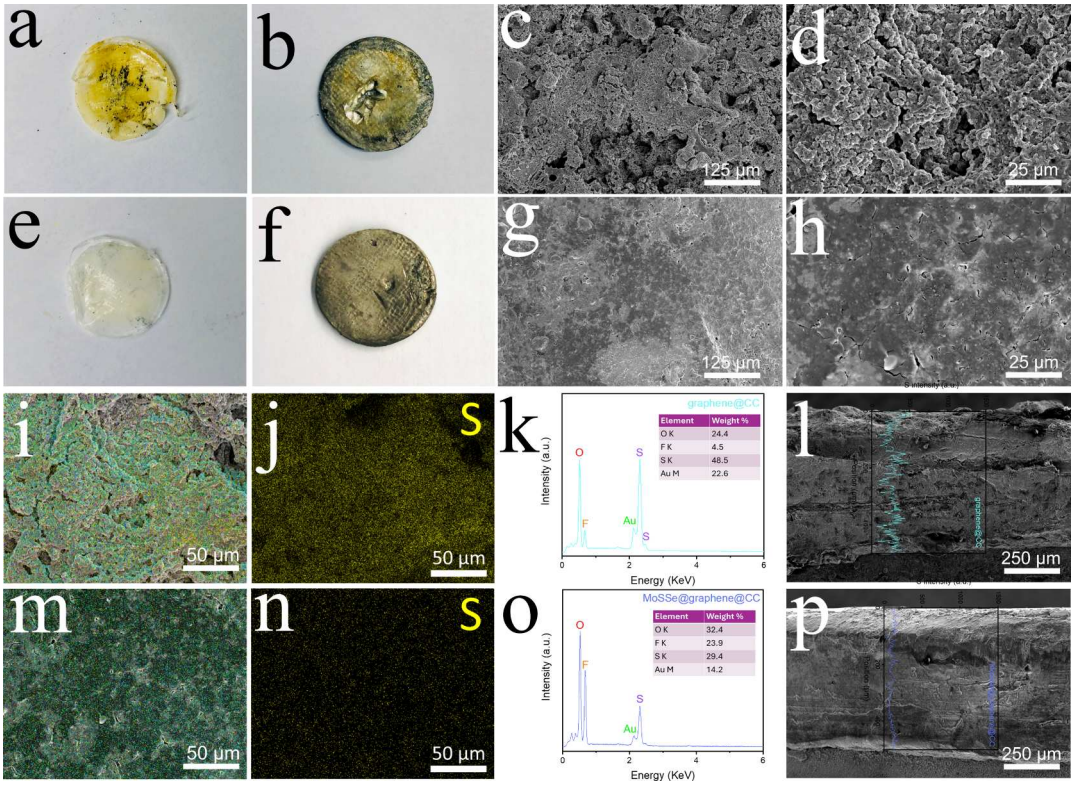

Fig. 10. The optical microscope photos of (a) the cycled separator and (b) the cycled Li anode; (c-d) SEM images, (i) EDS overlays, (j) EDS sulfur map (yellow), (k) EDS spectrum (the number of repeat experiments: 3), and (l) SEM cross-section image and EDS line scan profile of sulfur for the cycled Li anode from the graphene@CC cell. The optical microscope photos of (e) the cycled separator and (f) the cycled Li anode; (g-h) SEM images, (m) EDS overlays, (n) EDS sulfur map (yellow), (o) EDS spectrum (the number of repeat experiments: 3), and (p) SEM cross-section image and EDS line scan profile of sulfur for the cycled Li anode from the MoSSe@graphene@CC cell. (For interpretation of the references to color in this figure legend, the reader is referred to the web version of this article.)

Furthermore, the corrosion degree of Li metal anode was assessed by cross-sectional morphologies of the cycled Li metal anode paired with the MoSSe@graphene@CC cathode and the graphene@CC cathode. A corrosion thickness can be represented by the p sulfur species that migrated from the cathode to the anode. The graphene@CC cell (Fig. 10**l**) displays the Li metal anode with a corrosion thickness, which is much thicker than that with the MoSSe@graphene@CC cathode (Fig. 10**p**). These results as mentioned above verify the severe shuttle effect in the graphene@CC cell. The slight corrosion on the surface of Li metal anode paired with the MoSSe@graphene@CC cathode confirms the effective immobilization of polysulfide diffusion by polar MoSSe [77]. Therefore, these results further evidence that the additive selection and design with strong polysulfide adsorption and catalytic activity for the sulfur cathode are crucial for the electrochemical performance enhancement of Li-S battery [22,71,78,79].

4. Conclusion

In this work, sulfiphilic few-layered MoSSe nanoflakes were decorated on high surface area and highly conductive graphene (MoSSe@graphene) to optimize the binding energies of soluble polysulfides and guide the Li_2S nucleation and growth vertical to the interfacial surface. This nanohybrid structure can also mitigate the formation of the Li_2S passivation layer on the catalyst surface and allow for continuous Li^+ diffusion and subsequent nucleation of Li_2S. Owing to these beneficial features, Li–S cells with a MoSSe@graphene@CC electrode demonstrate remarkably enhanced electrochemical performance, including a high initial capacity of 1091 mAh g^{-1} at 1C and ultralong cycle stability with a low capacity decay rate of 0.040 % per cycle over 1000 cycles at 1C. This study offers an energy-efficient strategy (ultrafast microwave synthesis) to synthesize electrocatalytic host additive to control the Li_2S nucleation and growth and mitigate the shuttle effect of polysulfides, which provide a new processing route to fabricate highly efficient electrocatalysts for long-cyclable and high performance LSBs.

CRediT authorship contribution statement

Zhen Wei: Writing – original draft, Investigation, Formal analysis. **Shatila Sarwar:** Writing – review & editing, Investigation, Formal analysis. **Xinyu Zhang:** Writing – review & editing, Supervision, Resources, Methodology, Conceptualization. **Ruigang Wang:** Writing – review & editing, Writing – original draft, Validation, Supervision, Resources, Project administration, Methodology, Investigation, Funding acquisition, Formal analysis, Conceptualization.

Declaration of competing interest

The authors declare that they have no known competing financial interests or personal relationships that could have appeared to influence the work reported in this paper.

Data availability

No data was used for the research described in the article.

Acknowledgment

This work is supported by the National Science Foundation (CBET-2427263 and TI-2147564).

Appendix A. Supplementary data

Supplementary data to this article can be found online at https://doi.org/10.1016/j.jcis.2024.09.048.

References

[1] Y. Liang, Z. Wei, H.-E. Wang, M. Flores, R. Wang, X. Zhang, Flexible and freestanding PANI: PSS/CNF nanopaper electrodes with enhanced electrochemical performance for supercapacitors, J. Power Sources 548 (2022) 232071.
[2] Y. Liang, Z. Wei, R. Wang, X. Zhang, The Microwave Facile Synthesis of NiOx@graphene Nanocomposites for Application in Supercapacitors: Insights into the Formation and Storage Mechanisms, Coatings 12 (2022) 1060.
[3] W. Yao, J. Xu, Y. Cao, Y. Meng, Z. Wu, L. Zhan, Y. Wang, Y. Zhang, I. Manke, N. Chen, Dynamic intercalation–conversion site supported ultrathin 2D mesoporous SnO2/SnSe2 hybrid as bifunctional polysulfide immobilizer and lithium regulator for lithium–sulfur chemistry, ACS Nano 16 (2022) 10783–10797.
[4] L. Guo, B. Zhang, S. Li, A. Montgomery, L. Li, G. Xing, Q. Zhang, X. Qian, F. Yan, Interfacial engineering of oxygenated chemical bath–deposited CdS window layer for highly efficient Sb2Se3 thin-film solar cells, Materials Today Physics 10 (2019) 100125.
[5] M. Zhang, H. Du, Z. Wei, X. Zhang, R. Wang, Facile Electrodeposition of Mn-CoP Nanosheets on Ni Foam as High-Rate and Ultrastable Electrodes for Supercapacitors, ACS Applied Energy Materials 5 (2021) 186–195.
[6] M. Zhang, A. Nautiyal, H. Du, Z. Wei, X. Zhang, R. Wang, Electropolymerization of polyaniline as high-performance binder free electrodes for flexible supercapacitor, Electrochim. Acta 376 (2021) 138037.
[7] F. Sun, J. Wang, H. Chen, W. Li, W. Qiao, D. Long, L. Ling, High efficiency immobilization of sulfur on nitrogen-enriched mesoporous carbons for Li–S batteries, ACS Appl. Mater. Interfaces 5 (2013) 5630–5638.
[8] G. Zhou, L. Li, C. Ma, S. Wang, Y. Shi, N. Koratkar, W. Ren, F. Li, H.-M. Cheng, A graphene foam electrode with high sulfur loading for flexible and high energy Li-S batteries, Nano Energy 11 (2015) 356–365.
[9] G. Zhou, D.-W. Wang, F. Li, P.-X. Hou, L. Yin, C. Liu, G.Q.M. Lu, I.R. Gentle, H.-M. Cheng, A flexible nanostructured sulphur–carbon nanotube cathode with high rate performance for Li-S batteries, Energ. Environ. Sci. 5 (2012) 8901–8906.
[10] W. Zhou, Y. Yu, H. Chen, F.J. DiSalvo, H.D. Abruna, Yolk-shell structure of polyaniline-coated sulfur for lithium-sulfur batteries, J Am Chem Soc 135 (2013) 16736–16743.
[11] W. Yao, C. Tian, C. Yang, J. Xu, Y. Meng, I. Manke, N. Chen, Z. Wu, L. Zhan, Y. Wang, P-Doped NiTe2 with Te-Vacancies in Lithium-Sulfur Batteries Prevents Shuttling and Promotes Polysulfide Conversion, Adv. Mater. 34 (2022) 2106370.
[12] W. Yao, C. Chu, W. Zheng, L. Zhan, Y. Wang, "Pea-pod-like" nitrogen-doped hollow porous carbon cathode hosts decorated with polar titanium dioxide nanocrystals as efficient polysulfide reservoirs for advanced lithium–sulfur batteries, J. Mater. Chem. A 6 (2018) 18191–18205.
[13] G. Zhou, Y. Zhao, C. Zu, A. Manthiram, Free-standing TiO2 nanowire-embedded graphene hybrid membrane for advanced Li/dissolved polysulfide batteries, Nano Energy 12 (2015) 240–249.
[14] N. Hu, X. Lv, Y. Dai, L. Fan, D. Xiong, X. Li, SnO2/Reduced Graphene Oxide Interlayer Mitigating the Shuttle Effect of Li-S Batteries, ACS Appl Mater Interfaces 10 (2018) 18665–18674.
[15] W. Kong, L. Yan, Y. Luo, D. Wang, K. Jiang, Q. Li, S. Fan, J. Wang, Ultrathin MnO2/graphene oxide/carbon nanotube interlayer as efficient polysulfide-trapping shield for high-performance Li–S batteries, Adv. Funct. Mater. 27 (2017) 1606663.
[16] M. Liu, Q. Li, X. Qin, G. Liang, W. Han, D. Zhou, Y.B. He, B. Li, F. Kang, Suppressing self-discharge and shuttle effect of lithium–sulfur batteries with V2O5-decorated carbon nanofiber interlayer, Small 13 (2017) 1602539.
[17] H. Lin, N. Lou, D. Yang, R. Jin, Y. Huang, Janus MoSSe/graphene heterostructures: Potential anodes for lithium-ion batteries, J. Alloy. Compd. 854 (2021) 157215.
[18] X. Zheng, Y. Zhu, Y. Sun, Q. Jiao, Hydrothermal synthesis of MoS2 with different morphology and its performance in thermal battery, J. Power Sources 395 (2018) 318–327.
[19] D. He, Y. Yang, Z. Liu, J. Shao, J. Wu, S. Wang, L. Shen, N. Bao, Solvothermal-assisted assembly of MoS2 nanocages on graphene sheets to enhance the electrochemical performance of lithium-ion battery, Nano Res. 13 (2020) 1029–1034.
[20] X. Li, J. Li, Q. Gao, X. Yu, R. Hu, J. Liu, L. Yang, M. Zhu, MoS2 nanosheets with conformal carbon coating as stable anode materials for sodium-ion batteries, Electrochim. Acta 254 (2017) 172–180.
[21] A. Gowrisankar, A.L. Sherryn, T. Selvaraju, In situ integrated 2D reduced graphene oxide nanosheets with MoSSe for hydrogen evolution reaction and supercapacitor application, Applied Surface Science Advances 3 (2021) 100054.
[22] B. Yu, Y. Chen, Z. Wang, D. Chen, X. Wang, W. Zhang, J. He, W. He, 1T-MoS2 nanotubes wrapped with N-doped graphene as highly-efficient absorbent and electrocatalyst for Li–S batteries, J. Power Sources 447 (2020) 227364.
[23] B. Liu, Y. Liu, X. Hu, G. Zhong, J. Li, J. Yuan, Z. Wen, N-Doped Carbon Modifying MoSSe Nanosheets on Hollow Cubic Carbon for High-Performance Anodes of Sodium-Based Dual-Ion Batteries, Adv. Funct. Mater. 31 (2021) 2101066.
[24] W. Yao, S. Wu, L. Zhan, Y. Wang, Two-dimensional porous carbon-coated sandwich-like mesoporous SnO2/graphene/mesoporous SnO2 nanosheets towards high-rate and long cycle life lithium-ion batteries, Chem. Eng. J. 361 (2019) 329–341.
[25] X. Yu, G. Zhao, C. Wu, H. Huang, C. Liu, X. Shen, M. Wang, X. Bai, N. Zhang, Constructing anion vacancy-rich MoSSe/G van der Waals heterostructures for high-performance Mg–Li hybrid-ion batteries, J. Mater. Chem. A 9 (2021) 23276–23285.
[26] S. Zhang, Z. Huang, Z. Wen, L. Zhang, J. Jin, R. Shahbazian-Yassar, J. Yang, Local lattice distortion activate metastable metal sulfide as catalyst with stable full discharge–charge capability for Li–O2 batteries, Nano Lett. 17 (2017) 3518–3526.

[27] C. Hernández-Rentero, R. Córdoba, N. Moreno, A. Caballero, J. Morales, M. Olivares-Marín, V. Gómez-Serrano, Low-cost disordered carbons for Li/S batteries: A high-performance carbon with dual porosity derived from cherry pits, Nano Res. 11 (2018) 89–100.
[28] Z. Tian, N. Chui, R. Lian, Q. Yang, W. Wang, C. Yang, D. Rao, J. Huang, Y. Zhang, F. Lai, Dual anionic vacancies on carbon nanofiber threaded MoSSe arrays: a free-standing anode for high-performance potassium-ion storage, Energy Storage Mater. 27 (2020) 591–598.
[29] Q. Zhao, Q. Zhu, Y. An, R. Chen, N. Sun, F. Wu, B. Xu, A 3D conductive carbon interlayer with ultrahigh adsorption capability for lithium-sulfur batteries, Appl. Surf. Sci. 440 (2018) 770–777.
[30] Y. Zhang, X. Duan, J. Wang, C. Wang, J. Wang, J. Wang, Natural graphene microsheets/sulfur as Li-S battery cathode towards> 99% coulombic efficiency of long cycles, J. Power Sources 376 (2018) 131–137.
[31] Z. Wei, J. Li, Y. Wang, R. Wang, High-performance Li-S batteries enabled by polysulfide-infiltrated free-standing 3D carbon cloth with CeO2 nanorods decoration, Electrochim. Acta 388 (2021) 138645.
[32] Y. Yang, X. Li, R. Luo, X. Zhang, J. Fu, Y. Zheng, K. Huo, T. Zhou, A topochemically constructed flexible heterogeneous vanadium-based electrocatalyst for boosted conversion kinetics of polysulfides in Li–S batteries, Mater. Chem. Front. 5 (2021) 3830–3840.
[33] Z. Wei, J. Li, R. Wang, Surface engineered polar CeO2-based cathode host materials for immobilizing lithium polysulfides in High-performance Li-S batteries, Appl. Surf. Sci. 580 (2022) 152237.
[34] H. Zhao, B. Tian, C. Su, Y.J.A.A.M. Li, Interfaces, Single-atom iron and doped sulfur improve the catalysis of polysulfide conversion for obtaining high-performance lithium–sulfur batteries 13 (2021) 7171–7177.
[35] Z. Wei, R. Wang, Chemically etched CeO2-x nanorods with abundant surface defects as effective cathode additive for trapping lithium polysulfides in Li-S batteries, J. Colloid Interface Sci. 615 (2022) 527–542.
[36] S. Wu, W. Wang, J. Shan, X. Wang, D. Lu, J. Zhu, Z. Liu, L. Yue, Y. Li, Conductive 1T-VS2− MXene heterostructured bidirectional electrocatalyst enabling compact Li-S batteries with high volumetric and areal capacity, Energy Storage Mater. 49 (2022) 153–163.
[37] R. Wang, J. Yang, X. Chen, Y. Zhao, W. Zhao, G. Qian, S. Li, Y. Xiao, H. Chen, Y. Ye, Highly dispersed cobalt clusters in nitrogen-doped porous carbon enable multiple effects for high-performance Li–S battery, Adv. Energy Mater. 10 (2020) 1903550.
[38] M. Wang, L. Fan, X. Sun, B. Guan, B. Jiang, X. Wu, D. Tian, K. Sun, Y. Qiu, X. Yin, Nitrogen-doped CoSe2 as a bifunctional catalyst for high areal capacity and lean electrolyte of Li–S battery, ACS Energy Lett. 5 (2020) 3041–3050.
[39] L. Yang, Y. Li, Y. Wang, Q. Li, Y. Chen, B. Zhong, X. Guo, Z. Wu, Y. Liu, G. Wang, Nitrogen-doped sheet VO2 modified separator to enhanced long-cycle performance lithium-sulfur battery, J. Power Sources 501 (2021) 230040.
[40] B. Moorthy, S. Kwon, J.-H. Kim, P. Ragupathy, H.M. Lee, D.K. Kim, Tin sulfide modified separator as an efficient polysulfide trapper for stable cycling performance in Li–S batteries, Nanoscale Horiz. 4 (2019) 214–222.
[41] X. Qiu, Q. Hua, L. Zheng, Z. Dai, Study of the discharge/charge process of lithium–sulfur batteries by electrochemical impedance spectroscopy, RSC Adv. 10 (2020) 5283–5293.
[42] L. Zhou, D.L. Danilov, R.A. Eichel, P.H. Notten, Host materials anchoring polysulfides in Li–S batteries reviewed, Adv. Energy Mater. 11 (2021) 2001304.
[43] F. Zhou, Z. Li, X. Luo, T. Wu, B. Jiang, L.L. Lu, H.B. Yao, M. Antonietti, S.H. Yu, Low Cost Metal Carbide Nanocrystals as Binding and Electrocatalytic Sites for High Performance Li-S Batteries, Nano Lett 18 (2018) 1035–1043.
[44] Z. Wei, S. Sarwar, S. Azam, M.R. Ahasan, M. Voyda, X. Zhang, R. Wang, Ultrafast microwave synthesis of MoTe2@ graphene composites accelerating polysulfide conversion and promoting Li2S nucleation for high-performance Li-S batteries, J. Colloid Interface Sci. 635 (2023) 391–405.
[45] H. Zhang, L. Yang, P. Zhang, C. Lu, D. Sha, B. Yan, W. He, M. Zhou, W. Zhang, L. Pan, MXene-Derived TinO2n− 1 Quantum Dots Distributed on Porous Carbon Nanosheets for Stable and Long-Life Li–S Batteries: Enhanced Polysulfide Mediation via Defect Engineering, Adv. Mater. 33 (2021) 2008447.
[46] Y. Mo, J. Lin, S. Li, J. Yu, Anchoring Mo2C nanoparticles on vertical graphene nanosheets as a highly efficient catalytic interlayer for Li-S batteries, Chem. Eng. J. 433 (2022) 134306.
[47] J. Liu, C. Lin, Q. Xie, D.-L. Peng, R.-J. Xie, Core–shell zeolite imidazole framework-derived ZnSe@ CoSe2/C heterostructure enabling robust polysulfide adsorption and rapid Li+ diffusion in high-rate and high-loading lithium–sulfur batteries, Chem. Eng. J. 430 (2022) 133099.
[48] G. Liu, Q. Zeng, Z. Fan, S. Tian, X. Li, X. Lv, W. Zhang, K. Tao, E. Xie, Z. Zhang, Boosting sulfur catalytic kinetics by defect engineering of vanadium disulfide for high-performance lithium-sulfur batteries, Chem. Eng. J. 448 (2022) 137683.
[49] J.-L. Yang, D.-Q. Cai, X.-G. Hao, L. Huang, Q. Lin, X.-T. Zeng, S.-X. Zhao, W. Lv, Rich heterointerfaces enabling rapid polysulfides conversion and regulated Li2S deposition for high-performance lithium–sulfur batteries, ACS Nano 15 (2021) 11491–11500.
[50] B. Wang, L. Wang, B. Zhang, S. Zeng, F. Tian, J. Dou, Y. Qian, L. Xu, Niobium diboride nanoparticles accelerating polysulfide conversion and directing Li2S nucleation enabled high areal capacity lithium–sulfur batteries, ACS Nano 16 (2022) 4947–4960.
[51] Y. Cho, M. Jang, K.S. Lee, E. Lee, S.Y. Park, Y. Piao, The quinone-based conjugated microporous polymer as an effective electrode additive for activated graphene host material in lithium-sulfur batteries, Chem. Eng. J. 463 (2023) 142422.
[52] Z. Han, S. Zhao, J. Xiao, X. Zhong, J. Sheng, W. Lv, Q. Zhang, G. Zhou, H.M. Cheng, Engineering d-p orbital hybridization in single-atom metal-embedded three-dimensional electrodes for Li–S batteries, Adv. Mater. 33 (2021) 2105947.
[53] W. Yan, X. Gao, J.L. Yang, X. Xiong, S. Xia, W. Huang, Y. Chen, L. Fu, Y. Zhu, Y. Wu, Boosting Polysulfide Catalytic Conversion and Facilitating Li+ Transportation by Ion-Selective COFs Composite Nanowire for Li, S Batteries, Small 18 (2022) 2106679.
[54] S. Azam, Z. Wei, R. Wang, Cerium oxide nanorods anchored on carbon nanofibers derived from cellulose paper as effective interlayer for lithium sulfur battery, J. Colloid Interface Sci. 615 (2022) 417–431.
[55] S. Fahad, Z. Wei, A. Kushima, In-situ TEM observation of fast and stable reaction of lithium polysulfide infiltrated carbon composite and its application as a lithium sulfur battery electrode for improved cycle lifetime, J. Power Sources 506 (2021) 230175.
[56] X.M. Lu, Y. Cao, Y. Sun, H. Wang, W. Sun, Y. Xu, Y. Wu, C. Yang, Y., Wang, sp-Carbon-Conjugated Organic Polymer as Multifunctional Interfacial Layers for Ultra-Long Dendrite-Free Lithium Metal Batteries, Angew. Chem. (2024) e202320259.
[57] A. Mirtaleb, R. Wang, A highly stable and conductive cerium-doped Li7P3S11 glass-ceramic electrolyte for solid-state lithium–sulfur batteries, J. Am. Ceram. Soc. (2024).
[58] C. Zhang, Y. He, Y. Wang, Y. Liang, A. Majeed, Z. Yang, S. Yao, X. Shen, T. Li, S. Qin, CoFe2O4 nanoparticles loaded N-doped carbon nanofibers networks as electrocatalyst for enhancing redox kinetics in Li-S batteries, Appl. Surf. Sci. 560 (2021) 149908.
[59] T. Li, Y. Li, J. Yang, Y. Deng, M. Wu, Q. Wang, R. Liu, B. Ge, X. Xie, J. Ma, In Situ Electrochemical Activation Derived LixMoOy Nanorods as the Multifunctional Interlayer for Fast Kinetics Li-S batteries, Small 17 (2021) 2104613.
[60] P. Wu, L. Tan, X.-D. Wang, P. Liao, Z. Liu, P.-P. Hou, Q.-Y. Zhou, X.-J. Jin, M.-C. Li, X.-R. Shao, Porous 3D nitrogen-doped rGO/Co-Ni-S composite modified separator for high-capacity and stable lithium-sulfur batteries, Mater. Res. Bull. 145 (2022) 111550.
[61] M.-C. Li, Z. Liu, L. Tan, Q.-Y. Zhou, J.-J. Zhang, P.-P. Hou, X.-J. Jin, T.-B. Lv, Z.-Q. Zhao, Z. Zeng, Fabrication of cubic and porous carbon cages with in-situ-grown carbon nanotube networks and cobalt phosphide for high-capacity and stable lithium–sulfur batteries, ACS Sustain. Chem. Eng. 10 (2022) 10223–10233.
[62] Q.-Y. Zhou, L. Tan, T.-B. Lv, M.-C. Li, J.-J. Zhang, Z.-Q. Zhao, X.-J. Jin, Z. Liu, P.-P. Hou, Z. Zeng, Nickel Foam Coated by Ni Nanoparticle-Decorated 3D Nanocarbons as a Freestanding Host for High-Performance Lithium-Sulfur Batteries, ACS Appl. Mater. Interfaces 15 (2023) 3037–3046.
[63] Y. Zhang, Y. Cao, L. Fan, G. Shi, T. Zheng, H. Liu, J. Song, G. Gao, Structure-defined viologen-polyoxometalate modified separator dominating endurable Li-S batteries by a synergistic adsorption-electrocatalysis mechanism, Chem. Eng. J. 482 (2024) 148991.
[64] W. Yao, W. Zheng, K. Han, S. Xiao, Ultrathin double-shell nanotubes of narrow band gap titanium oxide@carbon as efficient polysulfide inhibitors towards advanced lithium–sulfur batteries, J. Mater. Chem. A 8 (2020) 19028–19042.
[65] W. Yao, W. Zheng, J. Xu, C. Tian, K. Han, W. Sun, S. Xiao, ZnS-SnS@ NC Heterostructure as robust lithiophilicity and sulfiphilicity mediator toward high-rate and long-life lithium–sulfur batteries, ACS Nano 15 (2021) 7114–7130.
[66] S. Hu, M. Yi, H. Wu, T. Wang, X. Ma, X. Liu, J. Zhang, Ionic-Liquid-Assisted Synthesis of N, F, and B Co-Doped CoFe2O4− x on Multiwalled Carbon Nanotubes with Enriched Oxygen Vacancies for Li–S Batteries, Adv. Funct. Mater. 32 (2022) 2111084.
[67] Q. Zeng, L. Xu, G. Li, Q. Zhang, S. Guo, H. Lu, L. Xie, J. Yang, J. Weng, C. Zheng, Integrating Sub-Nano Catalysts into Metal-Organic Framework toward Pore-Confined Polysulfides Conversion in Lithium-Sulfur Batteries, Adv. Funct. Mater. 2304619 (2023).
[68] S. Azam, Z. Wei, R. Wang, Adsorption-catalysis design with cerium oxide nanorods supported nickel-cobalt-oxide with multifunctional reaction interfaces for anchoring polysulfides and accelerating redox reactions in lithium sulfur battery, J. Colloid Interface Sci. 635 (2023) 466–480.
[69] C. Wei, M. Tian, Z. Fan, L. Yu, Y. Song, X. Yang, Z. Shi, M. Wang, R. Yang, J. Sun, Concurrent realization of dendrite-free anode and high-loading cathode via 3D printed N-Ti3C2 MXene framework toward advanced Li–S full batteries, Energy Storage Mater. 41 (2021) 141–151.
[70] M. Zhao, B.-Q. Li, X. Chen, J. Xie, H. Yuan, J.-Q. Huang, Redox comediation with organopolysulfides in working lithium-sulfur batteries, Chem 6 (2020) 3297–3311.
[71] Z. Shi, Z. Sun, J. Cai, X. Yang, C. Wei, M. Wang, Y. Ding, J. Sun, Manipulating electrocatalytic Li2S redox via selective dual-defect engineering for Li–S batteries, Adv. Mater. 33 (2021) 2103050.
[72] Z. Barlow, Z. Wei, R. Wang, Surface and defect engineered polar titanium dioxide nanotubes as an effective polysulfide host for high-performance Li-S batteries, Mater. Chem. Phys. 309 (2023) 128316.
[73] L.-W. Lin, M. Qi, Z.-T. Bai, S.-X. Yan, Z.-Y. Sui, B.-H. Han, Y.-W. Liu, Crumpled nitrogen-doped aerogels derived from MXene and pyrrole-formaldehyde as modified separators for stable lithium-sulfur batteries, Appl. Surf. Sci. 555 (2021) 149717.
[74] W. Liu, M. Lei, X. Zhou, C. Li, Heterojunction interlocked catalysis-conduction network in monolithic porous-pipe scaffold for endurable Li-S batteries, Energy Storage Mater. 58 (2023) 74–84.
[75] J. Xu, S. An, X. Song, Y. Cao, N. Wang, X. Qiu, Y. Zhang, J. Chen, X. Duan, J. Huang, Towards high performance Li–S batteries via sulfonate-rich COF-modified separator, Adv. Mater. 33 (2021) 2105178.
[76] Z. Shi, Z. Sun, J. Cai, Z. Fan, J. Jin, M. Wang, J. Sun, Boosting dual-directional polysulfide electrocatalysis via bimetallic alloying for printable Li–S batteries, Adv. Funct. Mater. 31 (2021) 2006798.

[77] Z. Barlow, Z. Wei, R. Wang, Boosting lithium polysulfide conversion via TiO2-supported niobium catalyst for lithium sulfur battery, Mater. Chem. Phys. 314 (2024) 128830.
[78] M. Wang, Z. Sun, H. Ci, Z. Shi, L. Shen, C. Wei, Y. Ding, X. Yang, J. Sun, Identifying the evolution of selenium-vacancy-modulated MoSe2 precatalyst in lithium–sulfur chemistry, Angew. Chem. Int. Ed. 60 (2021) 24558–24565.
[79] Y. Li, M. Wang, J. Sun, Molecular engineering strategies toward molybdenum diselenide design for energy storage and conversion, Adv. Energy Mater. 12 (2022) 2202600.